Observing, modeling, and interpreting magnetic fields of the solid Earth

Mioara Mandea (e-mail:mioara@ipgp.jussieu.fr)
Institut de Physique du Globe de Paris, 4, Place Jussieu, 75005 Paris, France

Michael Purucker (e-mail:purucker@geomag.gsfc.nasa.gov)
Raytheon ITSS at Planetary Geodynamics Lab, Goddard Space Flight Center, NASA, Greenbelt, MD 20771 USA

Received: 15 February 2005

Abstract.
Many Earth system processes generate magnetic fields, either primary magnetic fields or in response to other magnetic fields. The largest of these magnetic fields is due to the dynamo in the Earth's core, and can be approximated by a geocentric axial dipole that has decayed by nearly 10% during the last 150 years. This is an order of magnitude faster than its natural decay time, a reflection of the growth of patches of reverse flux at the core-mantle boundary. The velocity of the North magnetic pole reached some 40 km/yr in 2001. This velocity is the highest recorded so far in the last two centuries. The second largest magnetic field in the solid Earth is associated with induced and remanent magnetization within the crust. Controlled in part by the thermo-mechanical properties of the crust, these fields contain signatures of tectonic processes currently active, and those active in the distant past. Recent work has included an estimate of the surface heat flux under the Antarctic ice cap. In order to understand the recent changes in the Earth's magnetic field, new high-quality measurements are needed to continue those being made by Ørsted (launched in 1999), CHAMP and the Ørsted-2 experiment onboard SAC-C (both launched in 2000). The present paper is motivated by the advent of space surveys of the geomagnetic field, and illustrates how our way of observing, modeling, and interpreting the Earth's magnetic field has changed in recent years due to the new magnetic satellite measurements.

1. Introduction

The study of the geomagnetic field is one of the earliest of the geosciences, with observations made in classical times, and also is the subject of perhaps the first true scientific treatises. In 1269 Petrus Peregrinus wrote his "Epistola", an experimental discourse on a spherical lodestone, and made observations on the dipolar nature of the magnet, and its direction and magnitude (Smith, 1969). Three centuries later, William Gilbert's "De Magnete" applied this concept to the Earth. Observations were made through the second millennium for both scientific and practical (navigation) purposes, and Gauss had worked out the basis for a description of the geomagnetic field by the 1840's.

At present, measurement of the Earth's magnetic field is concerned with answering fundamental questions about the Earth's deep interior, its, litho-

sphere, the near-Earth environment, and with practical matters. Geomagnetic data are of great use in other geophysical studies, such as the mantle conductivity, the structure and thermo-mechanical properties of the crust, decadal-scale changes in the length-of-day, core-mantle coupling, and thermal core-mantle interactions. In the practical arena, models of the geomagnetic field are "burnt" onto computer chips for inclusion in space and ground navigation systems, frequently supplementing and complementing GPS navigation systems. The geomagnetic field is also used for directional drilling in the petroleum industry, because drilling-induced vibrations limit the utility of gyroscopic techniques.

Observations over more than one hundred years of the Earth's magnetic field describe its morphology and time-evolution. In this paper, a whirlwind tour of these spatial and temporal variations is given. The internal (core and crust) geomagnetic field and its variations is first described, then the external geomagnetic field and its variations, and the need for high-resolution data. Following this the geomagnetic data themselves are detailed, both from observatories and from satellites. The data themselves must be calibrated, and are typically subject to additional selection criteria prior to their inclusion in models. We discuss two modeling techniques, spherical harmonic analysis and equivalent source dipoles, which can be applied globally or regionally. In the last Section, new results obtained from measurements of the Earth's magnetic field are presented, including first order spatial and temporal characteristics, emphasizing core flow and lithospheric structure. Concluding are a list of unsolved problems, and proposed experiments/satellites which may serve to address them.

1.1. Temporal and spatial variations

The temporal variations of the geomagnetic field include timescales ranging from seconds to millions of years. These field variations are known to be of both external and internal origin. Within the solar system, the Sun's magnetic field dominates interplanetary space. An important characteristic of the Sun's magnetic field is its periodicity of about 11 years, known as the solar cycle. Streaming supersonically away from the Sun at velocities of 350-700 km/s is a plasma of neutral hydrogen atoms, protons, and electrons. The particles form the solar wind, governed by the equations of plasma physics (see, e.g. Kivelson and Russell, 1995). From the ionosphere surrounding the Earth out to about 10 Earth radii on the dayside, and more than 100 Earth radii on the nighside, is the magnetosphere (Figure 1), which keeps most of the solar wind particles out. A complicated system of currents exist in this region. The longitudinal drift of Van Allen radiation belt particles constitutes an electric current, the ring current, which decreases slightly the magnetic field observed at the Earth's surface. The ring current can be mathematically described as a

uniform continuously varying field with two harmonic overtones of periods 6 months and 1 year. This varying external field induces in the Earth electric currents which in turn produce an induced magnetic field. This induced magnetic field depends on the electrical conductivity of the crust and mantle, and extends to depths controlled by the skin effect.

At distances of more than two Earth radii, the magnetic field is very similar to that of a dipole situated at the center of the Earth, inclined by about 11° to the rotation axis (Figure 1). Lower in the ionosphere light from the Sun ionizes the atoms of the upper atmosphere; the sunlit hemisphere is much more conducting that the nighttime one. Strong electric currents circulate in the sunlit hemisphere, generating their own magnetic fields, with values at the earth's surface of up to 80 nT. These daily variations are called quiet-solar variations (Sq). The Sun is not always "quiet" and the daily variation can be obscured by much more energetic processes, known as magnetic storms (Figure 2).

On a scale of about half a year, the first internal variations are encountered. The field generated by the geodynamo process which takes place within the core is known as the "core" or "main" field. The time variations of this field, the "secular variation", mainly occur on decadal and longer timescales (Figure 3). Examination of geomagnetic data from worldwide magnetic observatories has revealed sudden changes of the trend of the secular variation, which have been named "geomagnetic jerks" or "secular variation impulses". These have been discussed by a number of authors (cf. Mandea et al., 2000).

The dipole part of the field is not static. On the same scales as the secular variation, the dipole moment of the Earth has been steadily decreasing since systematic intensity measurements began in the 1840's. Archeo-magnetic data suggest that the strength of the dipole part may fluctuate by a factor of 2, or even more. The most dramatic change in the core magnetic field are the excursions or the reversals of dipole direction. In recent epochs the dipole has been reversing on average every 10^6 years, but a glance at the well-known polarity scale shows considerable variability during the history of the geomagnetic field (Merrill et al., 1996).

At the Earth's surface the departure of the geomagnetic field from that of a dipole is very marked and has been known for 300 years (Halley, 1692). The magnetic features with scale lengths in excess of several thousand km are associated with the core field. On shorter scales the main source of the field is due to the magnetization of the crust (Figure 1). Some huge anomalies are well-known, such as Kursk in the Ukraine or Bangui in the Central African Republic; they extend over large areas with amplitudes reaching thousands of nT. Banded Iron Formations, and other rock types peculiar to the Proterozoic era, are common in surface exposures in these two regions. In the oceans, "striped" anomalies are associated with sea-floor spreading; this pattern is

characterized by a nearly constant direction over many hundred km, and can be correlated with the dipole reversal sequence over millions of years.

The movement of electrically conducting seawater through the Earth's main magnetic field generates secondary magnetic fields through the magnetohydrodynamic process of motional induction (Tyler et al., 1997). Although only a few nT in magnitude, the regularity of the lunar semidiurnal (M_2) tide has allowed it to be recognized (Tyler et al., 2003) in satellite magnetic field observations.

1.2. The new observational epoch

In order to describe these temporal and spatial variations, systematic surveys are necessary. Very important results obtained in recent decades are due to a new observational strategy involving the measurement of the geomagnetic field from satellite orbit. The first satellite to carry a magnetometer in orbit around the Earth was the Russian Sputnik 3 (1958). Beginning with the U.S. POGO satellites (1967-1971), global mapping of the intensity of the Earth's magnetic field began. In 1979, the U.S. satellite MAGSAT inaugurated the highly accurate mapping of the field components. MAGSAT data have been used to map the geomagnetic field from its largest scale (dipolar) to small scales (less than 1000 km). Unfortunately, no other MAGSAT-class mission flew during the next 20 years. In February 1999, the Danish Ørsted satellite was launched, soon followed by the German CHAMP (July 2000). Both of these missions map the vector field to an accuracy of a few nT. Other missions in this epoch include the Argentinian-US SAC-C (November 2000) satellite (magnitude only), and less accurate (vector-only) measurements from South African and Australian satellites. This series of missions created an era of continuous monitoring of the Earth's magnetic field from space, the "Decade of Geopotential Research", intended to last at least until the end of the present decade (see Section 6). In order to better separate spatial and temporal changes of the geomagnetic field, a three satellite ESA mission, Swarm, is now under development and scheduled for launch in 2009.

New results have come from this abundance of high-quality vector data. For the first time since MAGSAT, high-quality, globally-distributed vector magnetic field data are available. The quantity of data already dwarfs that of MAGSAT, and the resolution of the secular variation is significantly greater than for 1980 (Olsen, 2002; Langlais et al., 2003). There is also the tantalizing prospect of secular variation resolution beyond spherical harmonic degree 13 (Olsen et al., 2002). Recently, the difference between the 1980 and 2000 fields was used to compute more detailed flows at the core-mantle boundary (Wardinski and Holme, 2004), particularly to resolve polar vortices in the flow above the inner core tangent cylinder (Hulot et al., 2002).

2. Measuring the Earth's Magnetic Field

Measurements of the geomagnetic field are of two types: scalar and vector. Scalar magnetometers make measurements of the strength of the magnetic field only, and provide no information about its direction. These measurements are commonly made with resonance magnetometers such as proton precession magnetometers, cesium vapor magnetometers, or, more recently, helium magnetometers. The Overhauser magnetometer, a type of proton precession or resonance magnetometer, is typically installed at magnetic observatories on the Earth's surface, and is used on the Ørsted and CHAMP satellites. The measurement principle is based on nuclear magnetic and electron spin resonance, and the frequency of the induced output signal is proportional to the magnitude of the field. Overhauser magnetometers utilize significantly less power than classical proton magnetometers, and produce a continuous precession signal. These magnetometers are referred to as absolute instruments, because they rely on a well-determined, and invariant, physical constant, the gyromagnetic ratio of the proton. Helium magnetometers are another class of resonance magnetometers. They use the most common He^4 isotope, and utilize another well-determined constant, the electron gyromagnetic ratio of helium for their magnetic field determination. Recent reviews of the resonance technique, and spaceborne instrumentation, can be found in Primdahl (2000) and Acuña (2002). Vector magnetometers make measurements that are proportional to the strength of the magnetic field with respect to a principal axis in the sensing element. Such measurements are typically obtained using triaxial orthogonal arrangements of single axis fluxgate magnetometers. The measurement principle is based on applying an alternating magnetic field to a material of high magnetic permeability. The voltage induced in a pickup coil is measured, and the even harmonics are proportional to the ambient magnetic field in the direction of the sense winding. The magnitude and directional response of these instruments needs to be calibrated against accurately known sources. Recent reviews of these instruments can be found in Ripka (2001), Snare (1998) and Acuña (2002). In the following, the details of scalar and vector measurements on the ground at magnetic observatories and in space by satellite are discussed.

2.1. Magnetic observatories

The main difficulty in running a magnetic observatory arises from the different nature of absolute and variation measurements. A scalar measurement of the field intensity obtained by a proton magnetometer is absolute: this means that it depends only on the knowledge of a physical constant and a measurement of frequency, which can be achieved with great accuracy (in excess of 10 ppm). In contrast, a vector measurement made with a flux-

gate magnetometer is subject to instrument drift arising from sources both within the instrument (e.g. temperature effects) and also the stability of the instrument mounting. Because these measurements are not absolute, they are referred to as ”variation” measurements, and the instruments are referred to as ”variometers”. It is possible to make an absolute measurement of the direction of the geomagnetic field, but this can only be performed with a fluxgate-theodolite which requires manual operation and takes a number of minutes. At a land-based observatory, such absolute measurements are typically made twice a week and are used to monitor the drift of the fluxgate variometers. The fluxgate-theodolite measures the direction of the geomagnetic field with respect to the horizontal plane (inclination) and the angle in the horizontal plane between magnetic north and true north (declination).

Modern land-based magnetic observatories all use similar instrumentation to produce similar data products; for a full description, see Jankowski and Sucksdorf (1996) and also the Intermagnet web site[1]. The fundamental measurements recorded to fulfil Intermagnet quality requirements are the one-minute values of the vector components and of the scalar intensity. The one-minute data are important for studying variations of the geomagnetic field external to the Earth, in particular the daily variation and magnetic storms. From the one-minute data, hourly, daily, monthly and annual mean values are produced. The monthly and annual mean values capture the secular variation of the field emanating from the Earth’s core. The quality of the estimates of secular variation depend critically on the quality of absolute measurements at each observatory.

Another key parameter in determining the secular variation on a global scale is the observatory distribution. Installed mainly on continents, the magnetic observatories are very unevenly distributed, as shown in Figure 4. This is the reason why in some regions, as for example the Pacific, the uncertainty in the secular variation is on the order of hundreds of nT/yr (Mandea and Macmillan, 2000). The way to improve our knowledge of the secular variation is to have well-distributed global measurements provided by satellites.

2.2. Satellites for magnetic observations

The first satellite measurements provided total field intensity only. It was soon realized, however, that even with this better distribution of observations, a fundamental uncertainty remained. The knowledge, even perfectly, of the total field intensity on the Earth’s surface, does not characterize sufficiently well its geometry (Backus, 1970). Indeed, the differences in the field values obtained from two models based on vectorial data, or on scalar data only, might be as large as several thousand nT near the magnetic equator (“Backus effect“). To avoid this problem, satellites must make vector measurements. It

[1] http://www.intermagnet.org

is also necessary for these measurements, in a geocentric reference system, to be made with a very high accuracy.

Ørsted, CHAMP and SAC-C are the three currently operational satellites as of 2005. Only these satellites here are described here, as an extensive literature (cf. Langel and Hinze, 1998) exists on earlier satellites. Ørsted and CHAMP provide high-quality vector and absolute data, while SAC-C provides only absolute data. All three have their magnetometers on long, rigid booms in order to minimize spacecraft-generated fields, and are in polar orbits in order to provide global mapping of the magnetic field.

Ørsted[2] Ørsted, Denmark's first satellite, was named after the Danish physicist H.C. Ørsted, credited with the first experimental demonstration of the relation of electricity and magnetism. The Ørsted satellite was launched into an orbit with an inclination of $96.5°$, a period of 100 minutes, an apogee of 860 km, and a perigee of 650 km. It has a length of 8.72 m and a mass of 62 kg (Figure 5). Stability is provided by a gravity-gradient scheme with magnetotorquers for attitude control. Ørsted moves slowly through local time by virtue of this orbit, with a change of 0.91 minutes/day. The 8 m boom is of a deployable type. The absolute magnetometer is mounted on the end of the boom, and its vector magnetometer mounted 2 m closer to the satellite body. The vector magnetometer is located on an optical bench with a star camera. The error in the measurement angles from the single star camera is anisotropic by almost a factor of two, with a more accurate bore-sight direction, and a less accurate knowledge of the bore-sight rotation angle. Satellite location is done by a GPS receiver, provided by NASA's Jet Propulsion Laboratory (JPL), with an accuracy of 10 m or better. The absolute magnetometer is an Overhauser type, and measures the total field with an accuracy of better than 0.5 nT, at a sampling rate of 1 Hz. It was developed by Laboratoire d'Electronique de Technologie de l'Information (LETI) [3]. The vector magnetometer is a fluxgate, and uses the Compact Spherical Coil (CSC) design. It measures the field at rates from 100 Hz in the polar regions to 20 Hz elsewhere, with a resolution of 0.1 nT. It was developed by the Danish Technical University (DTU)[4] and the Danish National Space Center (DNSC)[5].

CHAMP[6] The German satellite CHAMP (CHAllenging Minisatellite Payload) measures both the Earth's magnetic and gravity fields. Launched into orbit 16 months after Ørsted, CHAMP is in a near-circular orbit with an inclination of $87.3°$, a period of 90 minutes, and an initial altitude of 454 km. It has

[2] http://www.dmi.dk/projects/oersted
[3] http://www-leti.cea.fr/uk/index-uk.htm
[4] http://www.dtu.dk/
[5] http://spacecenter.dk/
[6] http://op.gfz-potsdam.de/champ

a length of 8.33 m and an initial mass of 522 kg (Figure 5). CHAMP moves rapidly through local time, with a change of 5.45 minutes/day. Stability relies on a cold-gas propulsion system and its aerodynamic shape is for stringent three-axis control in the denser atmosphere encountered at low-altitudes. The boom is 4 m in length, with the absolute magnetometer mounted on the end of the boom, and the vector magnetometer located in the mid-boom region. The vector magnetometer is located on an optical bench with dual star cameras, resulting in a more isotropic determination of the error in the field direction than for Ørsted. Attitude is estimated to be accurate to 3 arc-seconds, corresponding to a 0.5 nT accuracy in the vector magnetic components. Like Ørsted, the absolute magnetometer is of an Overhauser type, the vector magnetometer is a CSC fluxgate, and the GPS is a JPL-provided Blackjack, with details as provided above.

SAC-C[7] Launched in the same year as CHAMP, SAC-C (Satelite Argentino de Observacion de la Tierra) is a joint Argentinian-US satellite which hosts a Danish-US magnetometry package. The Ørsted-2 experiment onboard SAC-C consists of an absolute magnetometer in a 702 km circular orbit at a fixed local time (Figure 5). The experiment also included a vector magnetometer, but a broken connection in a coaxial cable has prevented the acquisition of any vector data. SAC-C has an inclination of $98.2°$. The Sun-synchronous orbit crosses the equator at Local Times of 10:24 and 22:24. The boom is 8 m in length, with the absolute magnetometer mounted on the end of the boom. The absolute instrument is a Helium magnetometer, developed by NASA's JPL, and measures the total field with an accuracy of better than 4 nT before account is taken of spacecraft fields, at a sampling rate of 1 Hz.

3. From Measurement to Modeling

The large amount of high-quality data provided by the satellites and observatories serves as the basis for modeling. But there are two important steps that need to be performed prior to modeling: calibration, and data selection.

3.1. Alignment, calibration, and inter-calibration

Spaceborne vector magnetometers are aligned and calibrated by comparing their outputs with those of an absolute instrument (scalar calibration) or with that of a known magnetic field vector (vector calibration). Alignment refers to the determination of the three Euler angles describing the rotation between the magnetometer coordinates and the star camera coordinates, while calibration refers to the estimation of the magnetometer response. This is first done

[7] http://web.dmi.dk/fsweb/projects/oersted/SDC/sac-c.html

on the ground (Risbo et al., 2003), and later in orbit (Olsen et al., 2003). In the ideal case, one should be able to calibrate the vector magnetometer before flight, but differences of the order of arc-minutes are commonly encountered between ground and in-flight calibrations. These differences are commonly ascribed to 1) atmospheric diffraction effects encountered in ground calibrations using the star camera, 2) changes in the magnetometer system caused by the launch process, or encountered in the vacuum of space, and 3) aging and radiation degradation. Calibration is a continuous process, and is typically repeated at weekly to monthly intervals during the mission, while alignment is done only once. Calibration consist of determining the scale values, offsets, and non-orthogonalities. If the magnetic field vector is accurately known, then a vector calibration is superior to a scalar calibration. However, if the vector field model is known only approximately, as for example by a field model, then a scalar calibration is superior. However, a scalar calibration does not permit the determination of the alignment angles. For this purpose, it is necessary to use a field model. Finally, the responses of the multiple magnetometer systems (Ørsted, CHAMP, and SAC-C) need to be inter-calibrated. This is necessary because of the use of a different absolute instrument on SAC-C.

Following the development in Olsen et al. (2003), the magnetometer output $\mathbf{E} = (E_1, E_2, E_3)^T$ (in engineering units, eu) is connected to the applied magnetic field $\mathbf{B}_{CSC} = (B_1, B_2, B_3)^T$ (in an orthogonal magnetic axes system) via

$$\mathbf{E} = \underline{\underline{\mathbf{S}}} \cdot \underline{\underline{\mathbf{P}}} \cdot \mathbf{B}_{CSC} + \mathbf{b} \tag{1}$$

where

$$\mathbf{b} = \begin{pmatrix} b_1 \\ b_2 \\ b_3 \end{pmatrix}$$

is the vector of offsets (in eu),

$$\underline{\underline{\mathbf{S}}} = \begin{pmatrix} S_1 & 0 & 0 \\ 0 & S_2 & 0 \\ 0 & 0 & S_3 \end{pmatrix}$$

is the matrix of sensitivities (in eu/nT), and

$$\underline{\underline{\mathbf{P}}} = \begin{pmatrix} 1 & 0 & 0 \\ -\sin u_1 & \cos u_1 & 0 \\ \sin u_2 & \sin u_3 & \sqrt{(1 - \sin^2 u_2 - \sin^2 u_3)} \end{pmatrix} \tag{2}$$

is a matrix which transforms a vector from the orthogonal magnetic axes coordinate system to the non-orthogonal magnetic measurement system.

The 9 parameters $b_i, S_i, u_i,\ i = 1,2,3$ describe the response of a linear magnetometer. Three additional parameters, the Euler angles α, β, γ, transform the magnetic field vector $\mathbf{B}_{SIM}$ in the star imager coordinate system to the vector

$$\mathbf{B}_{CSC} = \underline{\underline{\mathbf{R}}} \cdot \mathbf{B}_{SIM} \tag{3}$$

in the CSC magnetometer system. The matrix $\underline{\underline{\mathbf{R}}}$ is given by

$$\underline{\underline{\mathbf{R}}} = \begin{pmatrix} \cos\alpha & -\sin\alpha & 0 \\ \sin\alpha & \cos\alpha & 0 \\ 0 & 0 & 1 \end{pmatrix} \begin{pmatrix} \cos\beta & 0 & \sin\beta \\ 0 & 1 & 0 \\ -\sin\beta & 0 & \cos\beta \end{pmatrix} \begin{pmatrix} \cos\gamma & -\sin\gamma & 0 \\ \sin\gamma & \cos\gamma & 0 \\ 0 & 0 & 1 \end{pmatrix}$$

Hence the connection between the sensor output $\mathbf{E}$ and the magnetic field $\mathbf{B}_{SIM}$ in the reference coordinate system of the star imager is given by

$$\mathbf{E} = \underline{\underline{\mathbf{S}}} \cdot \underline{\underline{\mathbf{P}}} \cdot \underline{\underline{\mathbf{R}}} \cdot \mathbf{B}_{SIM} + \mathbf{b}. \tag{4}$$

Once the calibration parameters are known, the magnetic field in the CSC and SIM coordinate system, respectively, can be determined from the sensor output by applying the relationships

$$\mathbf{B}_{CSC} = \underline{\underline{\mathbf{P}}}^{-1} \cdot \underline{\underline{\mathbf{S}}}^{-1} \cdot (\mathbf{E} - \mathbf{b}) \tag{5}$$

$$\begin{aligned} \mathbf{B}_{SIM} &= \underline{\underline{\mathbf{R}}}^{-1} \cdot \mathbf{B}_{CSC} \\ &= \underline{\underline{\mathbf{R}}}^{-1} \cdot \underline{\underline{\mathbf{P}}}^{-1} \cdot \underline{\underline{\mathbf{S}}}^{-1} \cdot (\mathbf{E} - \mathbf{b}) \end{aligned} \tag{6}$$

It follows from (5) that the scalar intensity B_{CSC} of the CSC magnetometer is related to the sensor output $\mathbf{E}$ by

$$B_{CSC} = |\mathbf{B}_{CSC}| = \sqrt{\mathbf{B}_{CSC}^T \cdot \mathbf{B}_{CSC}} \tag{7}$$

$$= \sqrt{(\mathbf{E} - \mathbf{b})^T \cdot \underline{\underline{\mathbf{S}}}^{-1} \cdot \left(\underline{\underline{\mathbf{P}}}^{-1}\right)^T \cdot \underline{\underline{\mathbf{P}}}^{-1} \cdot \underline{\underline{\mathbf{S}}}^{-1} \cdot (\mathbf{E} - \mathbf{b})}. \tag{8}$$

A linearized robust least-squares approach is used to evaluate this system of equations, using Huber weights to account for outliers. Olsen et al. (2003), using three years of Ørsted data, found that the agreement between the two magnetometers after calibration was 0.33 nT rms. The Euler angles describing the rotation between the magnetometer coordinate system and the reference system of the star imager were determined with an accuracy of better than 4 arcsec.

3.2. Data selection

The first step in exploiting satellite data is to validate their quality, for example by comparing the raw data with synthetic data provided by an independent field model, by imposing limits for the first and second derivative, or using a

wavelet technique (Langlais et al., 1999; Balasis, 2003). This process reduces the amount of raw data.

Magnetically quiet data are preferred for internal field modeling. This single step often reduces the amount of data by an order of magnitude. If the currents which normally exist in the ionosphere and magnetosphere are enhanced as a result of perturbations driven by interaction with the solar wind, they produce a change in the magnetic field. This change cannot be described by a global model based on data without parameters representing such currents, and the associated magnetic fields. The selection criteria have to be applied to both vector and scalar magnetometer data, and they have to be restrictive enough to include only magnetically quiet periods, but the criteria should also be expansive enough to ensure a dataset large enough to allow high degree and order spherical harmonic models to be derived. Although the main current axis of the polar electrojet is located at about 70° dipole latitude, vector field effects can be sensed to 50° dipole latitude. Hence, vector data generally are taken for dipole latitudes equatorward of $\pm 50^\circ$, and scalar data for regions poleward $\pm 50^\circ$, or if vector data are missing due to attitude determination problems.

To limit the contributions from ionospheric currents at middle and low latitudes, only the dawn side data are generally selected from the MAGSAT mission, and only night-side data from the Ørsted and CHAMP missions. However, the night-side criteria can be defined in different ways when selecting the effects of satellite data. Figure 6 shows the different night-side definitions (Chambodut et al., 2003), and Table 1 summarizes some of them, commonly used.

Table I. Some examples of selection criteria.

Holme et al. (2003)	18:00 -06:00 Local Time
Langlais et al. (2003)	North-to-South passes,with Local Time slowly decreasing from 03:00 - 20:00
Olsen et al. (2003)	Sun at least 5° below horizon (previous 19:00-07:00 LT)
Cain et al. (2003)	dusk to dawn for Ørsted
Chambodut et al. (2003)	real shadow side

To restrict the data to quiet times, Kp index (see Kivelson and Russell, 1995) is often used, specifically requiring small values for it. Considering a particular data with associated time t (hour), the criteria generally used are $Kp(t) \leq$

1^+, and for the previous three hour interval $Kp(t-3) \leq 2^-$. The values for this index can be retrieved from the World Data Center (WDC) for Geomagnetism[8] or associated websites.

To define periods when the large scale external field is weak and stable the Dst index is used, specifically requiring small values, as $|Dst| \leq 5$ nT, $|d(Dst)/dt| \leq 3$ nT·hour^{-1}. This index, measuring the state of the ring current. can also be retrieved from the WDC [9].

Data selection based on Local Time and geomagnetic indices removes many of the aperiodic and periodic magnetic variations of external origin. The impact of the choice of different selection criteria on the resulting internal field models has been investigated by Chambodut et al. (2003).

4. Modeling

4.1. Global modeling

Several parameterizations are in common use to describe the size and shape of a planetary magnetic field. Two of the most commonly used techniques, spherical harmonic analysis, and equivalent source dipoles, are described here. Other parameterizations, including those based on splines, wavelets, monopoles, and natural orthogonal polynomials, have also seen recent use (cf. Langel, 1987; O'Brien and Parker, 1993; Parker, 1994).

4.1.1. *Spherical Harmonic Modeling*

In a space defined by three spherical coordinates (r, θ, ϕ), the geomagnetic induction field $\vec{B}$ can be expressed as

$$\vec{B} = -\vec{\nabla} V \tag{9}$$

where V is a scalar potential satisfying $\Delta V = 0$. At the Earth's surface this potential is the sum:

$$V = V_i + V_e \tag{10}$$

where V_i and V_e represent the internal and external scalar potential.

Magnetic fields are more commonly defined by the value H, the magnetic field strength. In the terms expressed above, the induction vector, $\vec{B}$, is the gradient of the scalar field potential, pointing towards the maximum field potential. Given that the flux density, $\vec{B} = \mu_0 \vec{H}$, where μ_0 is the permeability of free space, we can substitute $\vec{B}$ for $\vec{H}$.

In spherical coordinates equation $\Delta V = 0$ can be written as

$$\frac{\partial}{\partial r}\left(r^2 \frac{\partial V}{\partial r}\right) + \frac{1}{r^2 sin\theta}\frac{\partial}{\partial \theta}\left(sin\theta \frac{\partial V}{\partial \theta}\right) + \frac{1}{r^2 sin^2\theta}\frac{\partial^2 V}{\partial \phi^2} = 0 \tag{11}$$

[8] http://swdcdb.kugi.kyoto-u.ac.jp/
[9] http://swdcdb.kugi.kyoto-u.ac.jp/dstdir/

and it is solved by separation of variables and then expanded into a spherical harmonic series (see below).

Harmonics are widely used in mathematics and physics to represent complex, usually natural, functions. These harmonics are periodic functions of varying amplitude and period. The more harmonics used, the closer will be the approximation to reality.

4.1.2. *Mathematical expression*

Following Gauss (1839), the two potentials V_i, V_e can be developed as spherical harmonic expansions:

$$V_i = a \sum_{n=1}^{N_i^{max}} \left(\frac{a}{r}\right)^{n+1} \sum_{m=0}^{n} \left(g_n^m \cos(m\phi) + h_n^m \sin(m\phi)\right) P_n^m(\cos(\theta)) \tag{12}$$

$$V_e = a \sum_{n=1}^{N_e^{max}} \left(\frac{r}{a}\right)^{n} \sum_{m=0}^{n} \left(q_n^m \cos(m\phi) + s_n^m \sin(m\phi)\right) P_n^m(\cos(\theta)) \tag{13}$$

$$+Dst \sum_{n=1}^{1} \left[\left(\frac{r}{a}\right)^{n} + Q_1 \left(\frac{a}{r}\right)^{n+1}\right] \sum_{m=0}^{n} \left(\tilde{q}_n^m \cos(m\phi) + \tilde{s}_n^m \sin(m\phi)\right) P_n^m(\cos(\theta))$$

where a is the radius of the Earth, $r \geq a$ denotes the radial distance of the observation from the center of the Earth, θ denotes the geocentric co-latitude, and ϕ denotes the East longitude for a given measurement location. $P_n^m(\cos\theta)$ are the Schmidt-normalized associated Legendre functions of degree n and order m. Measurements of the magnetic field, taken on ground or in space, are used to estimate the so-called Gauss spherical harmonic coefficients ((g_n^m, h_n^m) for internal sources, and (q_n^m, s_n^m) for external sources), in order to describe the geomagnetic field in a free-source region. Equations (12) and (13) are truncated to N_i^{max} and N_e^{max}, which correspond to $N_i(N_i+2)$ real internal coefficients, and, respectively, $N_e(N_e+2)$ real external coefficients. The coefficients $(\tilde{q}_1^0, \tilde{q}_1^1, \tilde{s}_1^1)$ account for the first degree and order Dst-dependent part of the external field, with its internal induced counterpart represented by Q_1. Alternative external field representations (cf. Olsen et al., 2002) are an area of active research.

Since the geomagnetic field changes in space and time, the Gauss coefficients are also time-dependent. In order to model time variations of internal origin, the secular variation, about one year of continuous observation is needed. This variation can be assumed to be constant over short time scales, and introduced in (12) by adding a secular-variation potential, V_{sv}, truncated to N_{sv}^{max}:

$$V_{sv} = a \sum_{n=1}^{N_{sv}^{max}} \left(\frac{a}{r}\right)^{n+1} \sum_{m=0}^{n} (t - T_0) \left(\dot{g}_n^m \cos(m\phi) + \dot{h}_n^m \sin(m\phi)\right) P_n^m(\cos(\theta)) \tag{14}$$

where $\dot{g}_n^m$, $\dot{h}_n^m$ denote the time derivative of the internal Gauss coefficients, T_0 the reference time (i.e., the epoch of the main-field model), and t is the considered time.

Usually the secular variation is neglected or solved only for the first eight degrees, as for IGRF models (Mandea and Macmillan, 2000). Solving (14) for the high-degree, low-energy terms is not easy because some aliasing occurs in both spatial and temporal domains, between crustal field and secular variation. In general the geomagnetic external variations, such as the daily variation, the apparent 27-day periodicity in magnetic activity, the semi-annual and annual variations, and the approximate 11-year period variations, are often neglected in (12) and (13).

4.1.3. *General solution*

The observed components (C_i^{obs}) of the ith magnetic field measurements $\vec{B}_i^{obs}$ are the northward (X_i^{obs}), eastward (Y_i^{obs}), downward vertical (Z_i^{obs}) components, and total intensity (F_i^{obs}). They are used to estimate the spherical harmonic coefficients, by minimizing the sum (Cain et al., 1967):

$$\chi^2 = \sum_{i=1}^{\mathbb{N}_{obs}} \omega_i^C \left(C_i^{obs} - C_i^{mod} \right)^2 \tag{15}$$

where C_i^{mod} is the corresponding field component derived from the model, $\mathbb{N}_{obs}$ is the number of observations, and ω_i^C denotes the weight associated with the ith measured component.

When considering an isotropic source of error, ω_i^C is commonly set to $1/\sigma_i^2$, where σ_i is the estimated measurement accuracy. This weighting scheme can be also expressed as a function of Local Time (to downweight dayside data), or of the geographical position (to downweight "noise" polar data). Identical weights are used whatever field component X, Y or Z is considered. This is the general approach applied to MAGSAT data, but not to Ørsted data.

For Ørsted, the poor determination of the rotation angle around the pointing axis ($\hat{n}$) of the Star Imager (SIM) leads to anisotropic uncertainties (Olsen et al., 2000). Resulting errors on the field components are thus anisotropic, which are taken into account by a weighting scheme developed by Holme and Bloxham (1996). $\vec{B}$, the observed magnetic field vector, and $\hat{n}$ can be used to define a new reference frame in which the errors on each field component can be expressed (provided their directions are not parallel). The new coordinate system is defined by $\vec{B}$, $\hat{n} \wedge \vec{B}$ and $\vec{B} \wedge (\hat{n} \wedge \vec{B})$, referred to as B, $B_\perp$ and B_3, respectively (Holme, 2000). The solution is obtained by solving (15), using the field components expressed in the new reference frame. Individual weights in this new coordinate system are:

$$\omega^B = \frac{1}{\sigma^2} \tag{16}$$

$$\omega^{B_\perp} = \frac{1}{\sigma^2 + (\hat{n} \wedge \vec{B})^2 \xi^2 + (\hat{n} \cdot \vec{B})^2 \psi^2} \tag{17}$$

$$\omega^{B_3} = \frac{1}{\sigma^2 + B^2 \psi^2} \tag{18}$$

where ψ^2 and ξ^2 are the error variances parallel and perpendicular to $\hat{n}$.

For a near-polar orbiting satellite, the number of data is larger near the poles than near the equator. Such an uneven coverage can be counterbalanced either by selectively decimating data along orbits or by downweighting data using a $\sin(\theta)$ factor, where θ is the colatitude.

4.1.4. *Equivalent source dipoles*

This technique was introduced by Mayhew (1979) for the representation of satellite magnetic field data. Using as input irregular and scattered magnetic measurements acquired on local or global scales, equivalent dipoles, uniformly located, can be used to predict the magnetic measurements in a least-squares fit. The location of the dipoles is often specified, thus reducing the number of parameters that must be specified for each dipole from six to three. Considering the magnetic moment M of a dipole located at (r_d, θ_d, ϕ_d), the magnetic potential observed at (r, θ, ϕ) is expressed as

$$V = -M \cdot \nabla \frac{1}{l} \tag{19}$$

This relation is valid provided that there are no sources between the dipole and the observation location. The distance l between the dipole and the observation location is written as:

$$l = \left(r_d^2 + r^2 - 2 r_d r \cos(\zeta) \right)^{\frac{1}{2}} \tag{20}$$

ζ being the angle between observation and dipole location:

$$\cos(\zeta) = \cos(\theta)\cos(\theta_d) + \sin(\theta)\sin(\theta_d)\cos(\phi - \phi_d) \tag{21}$$

The resulting magnetic field $\vec{B} = -\vec{\nabla} V$ is written as in 11. On the Earth, it is generally supposed that the magnetization anomaly is aligned along the direction of the main field (Langel and Hinze, 1998). In this case, it is only necessary to solve for the dipole moment M of the anomaly, its three components being written as ($M \sin I$, $M \cos I \cos D$, $M \cos I \sin D$), I and D being the inclination and the declination of the main magnetic field.

The geographical distribution of the dipoles should be as uniform as possible in order to minimize the magnetizations and any spatial aliasing. The uniformity can be tested using Runcorn's theorem (Runcorn, 1975) with a spherical shell and an internal dipole field. This should result in zero field. As shown by Purucker (2004), the polar coordinate subdivision (Katanfouroush

and Shahshahani, 2003) is superior to the icosahedral tessellation (Covington, 1993) in producing a uniform distribution.

The inverse problem (Purucker et al., 1996) can be written as:

$$\tilde{b} = \tilde{C}x + \tilde{\nu} \tag{22}$$

where $\tilde{b}$ is the vector containing the n magnetic observations (or the $3 \times n$ observed magnetic components), x is the vector containing the parameters of the m dipoles (the $3 \times m$ unknowns), and $\tilde{\nu}$ is the observation noise vector (of mean zero and covariance W^{-1}). $\tilde{C}$ is the geometric source function matrix between x and $\tilde{b}$, of size $3 \times n \times 3 \times m$. In order to normalize the noise, multiply (22) by $W^{1/2}$:

$$b = Cx + \nu \tag{23}$$

The inverse problem is solved by seeking the minimum of $L(x) = \nu^T \nu$, which corresponds to the normal equation

$$C^T C x = C^T b \tag{24}$$

When considering large problems, the computation of the product $C^T C$ can be very time consuming. It is then easier to use conjugate gradient approaches. Indeed the minimum for L is reached when $\nabla L = Cx - b$ goes to zero (Press et al., 1992) An iterative process is used where one computes for each step k a new solution x_{k+1} equal to $x_k + \alpha_k p_k$, where α_k is a scalar minimizing $L(x_{k+1})$ in the direction p_k:

$$\alpha_k = \frac{r_k^T r_k}{p_k^T C^T C p_k} \tag{25}$$

where r_k is the vector of the residuals after the kth iteration:

$$r_k = C^T b - C^T C x_k \tag{26}$$

By using the matrix identity $p_k^T C^T C p_k = (C p_k)^T C p_k$ in 25, one can use C directly instead of having to make to product $C^T C$. This is called the design matrix approach (Van der Sluis and Van der Horst, 1987). In order to ensure the convergence of the solution, C should be pre-conditioned (Tarantola, 1987).

4.2. Regional modeling

In cases where data are only available over a limited area of the Earth's surface, the spherical harmonic method presented above is no longer suitable. This is because the spherical harmonic expansion can not be made orthogonal over the restricted area. Two general approaches to regional modeling, polynomial modeling and spherical cap harmonic analysis, are widely used.

Recent extensions of the latter have allowed for a proper representation of the magnetic field.

4.2.1. *Polynomial modeling*

Common techniques, like polynomial modeling in latitude and longitude or rectangular harmonic analysis (Alldredge, 1981), have been successfully applied before the new satellite era. The data for this technique are provided by aeromagnetic and ship-borne magnetic surveys (obtained at different times with varied flight elevations, flight-line or track spacing, and data-reduction procedures) or for repeat station networks (obtained at different times and with a network more or less dense).

For each individual aeromagnetic and ship-borne magnetic survey, the total-intensity data are generally gridded at a variety of intervals depending on flight or track spacing. The geomagnetic reference fields (IGRF or DGRF, see section 5) for the areas of the surveys are subtracted from the total-intensity grids to produce the residual anomaly grids. After reducing data to a common datum, residual magnetic anomaly values in each survey are adjusted, if required, to minimize discontinuities at survey boundaries, and then each survey is merged to adjoining surveys. In general the data are then projected using a classical regional projection, and a second order polynomial normal field model is computed as:

$$C(\theta,\phi) = a_1+a_2(\theta-\theta_0)+a_3(\phi-\phi_0)+a_4(\theta-\theta_0)^2+a_5(\theta-\theta_0)(\phi-\phi_0)+a_6(\phi-\phi_0)^2 \tag{27}$$

for the magnetic component C at the point with latitude θ and longitude ϕ. The coefficients a_i are determined by a regression ($a_1[nT], a_2, a_3[1/nT], a_4, a_5, a_6[(1/nT)^2]$). The origin ($\theta_0, \phi_0$) is the center of the chosen region.

For magnetic repeat station surveys, full vector magnetic observations are made for a few hours, sometimes a few days, every few years (Newitt et al., 1996). In order to obtain final data, comparable with those provided by the geomagnetic observatories, specific data reduction methods have to be applied (Mandea Alexandrescu and Bitterly, 1999; Korte and Mandea, 2003). Maps can be derived using (27) or with simple interpolation schemes.

4.2.2. *Spherical Cap Harmonic modeling*

An attractive method in modeling the regional magnetic field is the spherical cap harmonic analysis (SCHA) proposed by Haines (1985, 1990). SCHA permits the use of data from only a portion of the Earth while satisfying the constraints of potential field theory. Indeed, the region to be studied has to be defined by a spherical cap; the analysis enables radial extrapolations and satisfies the zero curl and divergence conditions. The method is claimed to be valid over any spherical cap at any altitude above the Earth's surface. On the

basis of these assertions, SCHA has been widely used for producing magnetic anomaly maps (De Santis et al., 1997; Hwang and Chen, 1997; Korte and Haak, 2000).

The potential in spherical cap harmonics, including internal and external coefficients is expressed as:

$$\begin{aligned} V(r,\theta,\phi) &= a \sum_{k\geq 0} \sum_{m\geq 0} \left(\tfrac{a}{r}\right)^{n_k+1} \left(G_{n_k}^{i,m}\cos(m\phi) + H_{n_k}^{i,m}\sin(m\phi)\right) P_{n_k}^m(\theta) \\ &+ a \sum_{k\geq 0} \sum_{m\geq 0} \left(\tfrac{r}{a}\right)^{n_k} \left(G_{n_k}^{e,m}\cos(m\phi) + H_{n_k}^{e,m}\sin(m\phi)\right) P_{n_k}^m(\theta) \end{aligned} \quad (28)$$

However, when using this approach, two kinds of difficulties are commonly encountered. The first one comes from the failure to model correctly the radial dependence, implying that the models can not be upward or downward continued, and data acquired at different altitudes can not be inverted simultaneously. The second is that there is a tradeoff between the resolution of the vertical and horizontal components of the magnetic field.

4.2.3. *A new approach to SCHA*

A new proposal for spherical cap harmonic modeling has been proposed by Thebault et al. (2004). The problem is now solved inside a closed conical volume. Outside the source, the potential V satisfies the Laplace equation. The boundary conditions on each surface give the complete boundary value problem:

$$\begin{aligned} \Delta V &= 0 \\ V|_{\partial\Omega_\theta} &= F(r,\phi) \\ \left.\frac{\partial V}{\partial n}\right|_{\partial\Omega_a} &= G_1(\theta,\phi) \\ \left.\frac{\partial V}{\partial n}\right|_{\partial\Omega_b} &= G_2(\theta,\phi) \end{aligned} \quad (29)$$

where $\partial\Omega_\theta$ is the lateral boundary surface of the cone, as defined as $\theta = \theta_0$ and $a < r < b$ (a is the Earth's mean radius and b is the upper radius, for example $b \sim 7270$ km for Ørsted data). The initial problem may be decomposed into two sub-problems having either homogeneous Neuman or Dirichlet boundary conditions. The decomposition is not obviously unique, and Thebault et al. (2005) proposed the most intuitive one. Considering $V = V_1 + V_2$, the boundary value problem becomes:

$$\begin{aligned} \Delta V_1 &= 0 \\ V_1|_{\partial\Omega_\theta} &= F(r,\phi) \\ \left.\frac{\partial V_1}{\partial r}\right|_{\partial\Omega_a} &= 0 \end{aligned}$$

$$\left.\frac{\partial V_1}{\partial r}\right|_{\partial\Omega b} = 0 \tag{30}$$

$$\begin{aligned}
\Delta V_2 &= 0 \\
\partial V_2|_{\partial\Omega_\theta} &= 0 \\
\left.\frac{\partial V_2}{\partial r}\right|_{\partial\Omega_a} &= G_1(\theta,\phi) \\
\left.\frac{\partial V_2}{\partial r}\right|_{\partial\Omega b} &= G_2(\theta,\phi)
\end{aligned} \tag{31}$$

The solution for the potential V_1 is given by:

$$V_1(r,\theta,\phi) = a\sum_{p\geq 0}\sum_{m\geq 0} R_p(r)\left(G_p^m\cos(m\phi) + H_p^m\sin(m\phi)\right)K_p^m(\theta) \tag{32}$$

where the $K_p^m(\theta)$ are Mehler (conical) functions and the $R_p(r)$ are solutions of a Sturm-Liouville problem (see Thebault et al. (2004) for details). These solutions are appealing because they form an orthogonal basis, and appropriate radial representations can be developed in r^n with a given integer n, facilitating upward and downward continuation.

The solution for the potential V_2 is given by:

$$\begin{aligned}
V_2(r,\theta,\phi) = {} & a\sum_{k\geq 0}\sum_{m\geq 0}\left(\frac{a}{r}\right)^{n_k+1}\left(G_{n_k}^{i,m}\cos(m\phi) + H_{n_k}^{i,m}\sin(m\phi)\right)P_{n_k}^m(\theta) \\
& + a\sum_{k\geq 0}\sum_{m\geq 0}\left(\frac{r}{a}\right)^{n_k}\left(G_{n_k}^{e,m}\cos(m\phi) + H_{n_k}^{e,m}\sin(m\phi)\right)P_{n_k}^m(\theta)
\end{aligned} \tag{33}$$

This expression is similar to the well-known one describing the global potential.

This new mathematical formalism for SCHA is able to model the radial variation of the field properly, opening new directions in describing the Earth's magnetic field at regional scales from both surface and satellite data.

5. Results

5.1. Modeling of the core magnetic field and its variations

A precise survey of the Earth's magnetic field is of particular interest in the field of geophysical studies. With the new satellite missions, presented previously, a new impetus to the study of core and crustal fields has been generated.

Now that new magnetic satellite data are available, providing global coverage, it is important to review the results obtained and the improvements made in modeling techniques.

First Ørsted models The first published model using magnetic measurements taken by the Ørsted satellite was the *Ørsted Initial Field Model (OIFM)* (Olsen et al., 2000). For this model magnetic data obtained during geomagnetic quiet conditions around 1 January 2000 were used to derive a spherical harmonic model of the Earth's magnetic field for epoch 2000.0. The maximum degree/order of the model was 19 for internal, and 2 for external, source fields; however, coefficients above degree 14 may be not robust. Achieved rms misfit was 2 nT for the scalar intensity and 4 nT for the vector components perpendicular to the magnetic field.

The technique of utilizing the secular variation itself has been adopted for the derivation of the *Ørsted Main and Secular Variation Model (OSVM)* (Olsen, 2002). For this model the high-precision geomagnetic measurements from the Ørsted satellite have been used. However, in order to take full advantage of the improved data accuracy, the author refines the usual way of deriving field models from satellite data. A spherical harmonic model of the main field (up to degree/order 29) and of the secular variation (up to degree/order 13) is derived using Ørsted data spanning more than two years (March 1999 to September 2001) and applying new modeling approaches for a correct statistical treatment of the data errors and for considering external field contributions. Magnetospheric contributions are modeled up to degree/order 2; the zonal terms vary with annual and semi-annual periodicity, and the first terms are modulated with the strength of the magnetospheric ring-current as measured simultaneously by geomagnetic observatories. In addition, the observatory data are used to constrain the secular variation. The model is estimated using Iteratively Reweighted Least Squares with Huber weights to account for the non-Gaussian data error distribution. The rms misfit was 2.9 nT for the scalar intensity and for one of the vector components perpendicular to the magnetic field; the third vector component (rms misfit of 6.4 nT due to attitude noise) is down weighted when estimating the model.

The flurry of interest opened by the availability of Ørsted data is clear by the number of models published on different data sets and with different techniques (Neubert et al., 2001). Figures 7 and 8 show, as an example, the core field components (X, Y, Z) and their secular variation $(\dot{X}, \dot{Y}, \dot{Z})$ at the Earth's surface. One important application of these models is the study of the secular variation between two widely separated satellite epochs, e.g. MAGSAT and Ørsted.

MAGSAT - Ørsted secular variation Using satellite data and a set of selection criteria Langlais et al. (2003) computed two core field models (for

MAGSAT and Ørsted epochs) and a mean secular variation (over 20 years). To compute models which would be comparable, identical selection criteria were applied to MAGSAT and Ørsted data. However, as MAGSAT lasted only 7 months, it is difficult to compute the secular variation over such a short period. A few studies dealing with secular variation models computation using only satellite data have been published (Cain et al., 1983; Barraclough, 1985). Opposing views on using satellite data for secular variation have been expressed. In their study, Langlais et al. (2003) used only two months of data from MAGSAT, from 3 November through to 31 December 1979. On the contrary for Ørsted, all vectorial data in 1999 and all scalar data from March 1999 up to February 2000 inclusive have been used. The field models were derived using a least squares method (Cain et al., 1967). The mean secular variation model was computed as the normalized difference between the two models over 20 years. Both models are computed up to degree/order 20 for internal part and up to 2 for external part. For the Ørsted model a first-order temporal variation was allowed.

First CHAMP models Holme et al. (2003) produced a model *CO2* - CHAMP magnetic field model - created specifically to be used with data from the CHAMP satellite, valid for the initial period of the CHAMP mission (July 2000 - December 2001). The model contains internal field, linear secular variation and external field contributions. Although CHAMP data provide the most important input to the modeling, Holme et al. (2003) also use data from other satellites (Ørsted and SAC-C) and ground-based observatories, to increase the robustness of the model. The main field model and its secular variation estimate appear to be robust. However, the model of the external field is inadequate.

Analysis of the Ørsted, CHAMP and SAC-C magnetic field constellation Olsen et al. (2002) have improved the modeling strategy of the previous field models (like *OIFM, OSVM, CO2*) to derive a new model. The model parameterization follows that of previous models (especially *OSVM* and *CO2*), but with minor modifications. The spherical harmonic expansion of core and crustal fields now extends to degree/order 49, and the linear secular variation up to degree/order 16. The rms misfit of the scalar residuals at polar latitudes is much smaller than that of the *CO2* model, due to the improved data selection procedure (data from non-sunlit areas instead of selection according to Local Time). The non-polar scalar residuals are below 3 nT, due to the parameterization of the temporal variation of magnetospheric sources using SAC-C observations (an index called *RCsat* by Olsen (2002)) instead of *Dst*. This also has a positive influence on the vector residuals, despite the fact that the present model includes vector data from higher latitudes (for which one would expect larger residuals).

Recent IGRF/DGRF models A group of geomagnetic field modelers associated with the International Association of Geomagnetism and Aeronomy (IAGA)[10], periodically examines various geomagnetic field models from which the Earth's main field and its secular variation can be computed. These models now cover the period from 1900 to the present, and record the ongoing decay of the dipole field that can be seen in the historical record of the field (Jackson et al., 2000) since absolute measurements were first initiated in the 1840's. The working group produces a set of coefficients to represent the main field at a particular epoch, usually every five years, and name it the International Geomagnetic Reference Field (IGRF). Also, if a previous IGRF is re-derived using new data not available at the time of its first production and it is agreed that no additional data are likely to emerge, it is called a Definitive Geomagnetic Reference Field (DGRF). Beginning with epoch 2000.0 a new situation emerged because of the successful launch and operation of the Ørsted satellite. For the first time, the new IGRF main field model was based on satellite data only. Observatory data was subsequently added. Ørsted brought about an important change in IGRF/DGRF philosophy. Now labeled by their revision number, the coefficients of the tenth-generation IGRF are available in digital form from the IAGA web site[11] along with software to compute magnetic field values from them. The new coefficients are the main field coefficients for 1995.0 and 2000.0 (these are now definitive, and thus a DGRF), the main field coefficients for 2005.0 (an IGRF), and the secular-variation coefficients for 2005.0-2010.0. In order to ensure that the accuracy of the IGRF reflects the high quality of available satellite data, IAGA decided that for 2000.0 and subsequent epochs the main field coefficients should extend to degree 13 and be quoted to 0.1 nT precision (to reflect improved instrument resolution).

Comprehensive modeling For studies of the Earth's interior it is essential that internal field models be uncontaminated by external fields. The separation problem is complicated by the fact that, as seen from satellite altitudes, the ionospheric field, situated around 110 km altitude, behaves as an internal component. For the terrestrial magnetic observatories that same ionospheric field is seen as an external contribution. Recent investigations have shown a great advantage in modeling the Earth's internal fields (from the core and the crust), the core field secular variation, and the ionospheric and magnetospheric contributions simultaneously. This "Comprehensive approach" can be realized by means of a joint inversion of ground-based and satellite magnetic field measurements, as for example Sabaka et al. (2002; 2004) have done. Analysis of both surface and satellite data could theoretically resolve parameterizations of all sources, but only if the parameter set is treated consistently

[10] http://www.ngdc.noaa.gov/IAGA/vmod/igrf.html
[11] http://www.iugg.org/IAGA

between data types, which implies that they be co-estimated. Figure 9 shows an example of a comprehensive approach indicating the residual progression after each component field is removed. Models of this kind could provide the reference fields needed in more refined studies where source contamination is an issue. As a consequence, these types of models can be used to study features of the field such as geomagnetic jerks (Chambodut and Mandea, 2005) or to estimate core flow models at the core- mantle boundary.

The success of comprehensive modeling is in part driven by its utility to the scientific community. The method of co-estimating fields from several sources and its effect on model consistency is of scientific interest in its own right; however, additional merit of comprehensive models lies in their use as application tools, or reference models. Indeed, with the possible exception of the high degree lithospheric field where new, physically meaningful features might be found, most source fields are parameterized in such a way as to model the well known, regular, quiet time features. Hence, comprehensive models are well qualified to remove known fields from the data and therefore to avoid obfuscating that which is unknown.

5.2. Core flow modeling

The essence of the core field lies in electromagnetic induction-the association of electric currents and fields through the motion of a conducting fluid across magnetic field lines. The Earth's core is a highly conductive medium where convection takes place with characteristic velocities $\vec{u}$ of a few tens of km/year, i.e., five orders of magnitude larger than the assumed mantle convection (Stacey, 1992). The secular variation $(\partial\vec{B}/\partial t)$ is controlled by the induction equation:

$$\frac{\partial\vec{B}}{\partial t} = \vec{\nabla} \wedge (\vec{u} \wedge \vec{B}) + (\mu\sigma)^{-1}\Delta\vec{B} \tag{34}$$

On the right-hand side, the first term corresponds to advection, and the second one to diffusion. Diffusion, is controlled by the coefficient $\eta = \mu\sigma$, which in turn depends on the electrical conductivity σ and the permeability μ of the core. So, flow models of the top of the core can be derived from geomagnetic secular variation models of the radial magnetic field. However, the problem of non-uniqueness appears, because many different flows can generate the same secular variation and because of the non-uniqueness associated with non-perfect data. Resolving the non-uniqueness is possible if some hypotheses are assumed. The first is to compute large-scale flow using the frozen-flux hypothesis (Roberts and Scott, 1965). Indeed, on time scales shorter than a decade, and for medium to large spatial scales, the core may be considered to behave as a perfect conductor. The main consequence is that the magnetic field appears as frozen in the material of the core, the advection term

dominating the diffusion one:

$$\frac{\partial \vec{B}}{\partial t} \approx \vec{\nabla} \wedge (\vec{u} \wedge \vec{B}) \tag{35}$$

Some more hypotheses have to be made on the flow itself, for example, flows which are steady, steady in a drifting frame, tangentially geostrophic or purely toroidal. The flow model presented in the following is obtained by using the geostrophic approximation (Le Mouël, 1984; Gire et al., 1984; Gire and Le Mouël, 1990), which has been supported by some computations performed locally at the core-mantle boundary (Chulliat and Hulot, 2000). Using the radial component of the field, (35) becomes:

$$\frac{\partial B_r}{\partial t} = -\vec{\nabla}_H \cdot (\vec{u}\vec{B}_r) \tag{36}$$

and incorporating the tangentially geostrophic assumption

$$\vec{u} = \frac{1}{2\rho\Omega_0 cos\theta}\vec{n} \wedge \vec{\nabla} p \tag{37}$$

hence

$$\vec{\nabla}_H(\vec{u}cos\theta) = 0, \tag{38}$$

where $\vec{u}$ is the horizontal velocity field at the surface of the core (of the main stream), ∇_H is the gradient operator reduced to horizontal coordinates, θ is the co-latitude, ρ is the core density, Ω_0 is the Earth's mean rotation rate, $\vec{n}$ is the unit outward radial vector and ∇p is the pressure gradient.

Consequently, the radial component and its secular variation downward-continued to the core-mantle boundary (Figure 10) can be used to derive the flow at the top of the core, under these specific assumptions. The evolution of the B_r core field component between 1980 and 2000 (observed by the MAGSAT and Ørsted missions, respectively) was used to derive 20-year averaged small-scale flows (Hulot et al., 2002). These flows (Figure 11) proved to be very useful in providing insight into the geodynamo mechanism. Other studies rely on such fluid flow models. For example, the core axial angular momentum can be estimated and shown to account for the length-of-day variation on decadal time scales through exchange of axial angular momentum between the solid mantle and the core (Jault et al., 1988; Jackson et al., 1993; Pais and Hulot, 2000). More generally, the core is a place where many phenomena occur on decadal and shorter time scales. For example, there are the so-called torsional oscillations, which play a central role in core dynamics. These oscillations carry the core angular momentum (Jault et al., 1996), and could also be responsible for geomagnetic jerks (Bloxham et al., 2002). The dynamics of geomagnetic jerks have so far only been studied from ground-based observations (Mandea et al., 2000), because none has yet

occurred during a magnetic mapping mission. The rapid movement of the North magnetic pole, some 40 km/yr in 2001 (Newitt et al., 2002), may be related to such events (Mandea and Dormy, 2003).

Improving the core flow models depend first on improvements to the secular variation models. For the first time since MAGSAT, high-quality, globally distributed vector magnetic field data are available, and the resolution of the secular variation is significantly better than for 1980, beyond spherical harmonic degree 13. While the lithospheric field hides the core field at such wavelengths, if the surface field is very slowly varying in time (as is believed), then changes in the field at these shorter wavelengths can give us very useful information about core processes. Such higher resolution secular variation will lead to higher resolution flow models, or the observation of magnetic diffusion at the core surface, i.e. departures from frozen-in flux. The possibility of resolving sub-decadal secular variation, and consequently probing links with Earth's rotation on these shorter time scales, is also an open question. Significant new insights can be expected into the kinematics and dynamics of the core in the coming years by continuously observing the magnetic field from space and on the ground. ,

5.3. Lithospheric field

Near-Earth satellite missions have greatly enhanced our global and regional knowledge of the magnetization of the crust and uppermost mantle[12] For example, the MAGSAT vector data showed clearly, for the first time, that there was a major break in the power spectrum near spherical harmonic degree 13 (Langel and Estes, 1985). This break is interpreted to represent the change from dynamic core processes to quasi-static lithospheric ones (Figure 12). The magnitude of the crustal field, up to 25 nT at a satellite altitude of 400 km, can be explained by magnetizations of a few A/m distributed through a crustal thickness of 40 km. Based on thermal considerations, and high quality petrophysical compilations in the Scandinavian shield, remanent magnetization may dominate in the upper continental and oceanic crust, while induced magnetizations are thought to be dominant in the middle to lower crust. The base of the crust is thought to be a mineralogical boundary, with iron dominantly in oxide phases in the crust and in silicate phases in the mantle. This implies that the Moho is also a magnetic boundary (Wasilewski and Mayhew, 1992), with magnetization concentrated in the crust. The magnetic field originating from the lithosphere appears globally weaker in the oceanic domain than above continental areas. This probably reflects the factor of five

[12] We use the term 'lithosphere' in a thermal sense, to include crust and upper mantle rocks whose temperature is below the Curie point of the dominant magnetic phase, typically about 600° C. We often use the term 'crust' instead of 'lithosphere' when magnetizations are thought to be restricted to the crust.

difference in thickness between continental and oceanic crust, suggesting that lateral variations in magnetization and susceptibility are subordinate to thickness variations as a cause of magnetic anomalies.

Because the resolved lithospheric field contains only wavelengths less than 2800 km, maps of the field can be interpreted in terms of edge effects (Purucker et al., 2002). The resolution of the satellite data is sufficient to resolve only the widest sea-floor stripes, those associated with the Cretaceous quiet zones, although the satellite data are also capable of resolving the enhanced magnetization associated with spreading ridges. Measurements of the lithospheric field have been used for structural interpretations, for example to show that the Tornquist-Teisseyre structure running NW-SE through central Europe is a first-order feature characteristic of both the upper and lower crust. Lithospheric field measurements have also been used to delineate the thermomechanical properties of the lithosphere. For example, in the Java trench, a series of subduction parallel magnetic features (Maus et al., 2002) suggest that the subducted slab may retain some magnetization, and hence is cooler than the magnetite blocking temperature. Finally, if thickness variations in continental crust are a dominant factor in the creation of long-wavelength anomalies, solution of the heat conduction equation allows for an estimate of the surface heat flux (Fox Maule et al., 2003). Terrestrial heat flux is difficult to measure in many areas, especially in ice-covered regions, where a regional measure of surface heat flux has societal implications for the long-term stability of ice sheets.

Although these accomplishments are exemplary, outstanding problems remain. For example, there exists no global map of the crustal magnetic field! What exists are a patchwork of local to continental-scale compilations of marine and aeromagnetic data, and global maps of the satellite field (Maus et al., 2005). The World Digital Magnetic Anomaly Map (Ravat et al., 2003), based on a 5 km grid, is designed to fill that gap by 2007. Techniques which show promise in combining the satellite and near-surface data (cf Figure 13) include splines (Purucker and Whaler, 2003) and spherical-cap harmonic analysis (Thebault et al., 2004, 2005).

In addition, two source fields remain undetermined: the longest wavelength crustal fields that overlap with the core, and the shortest wavelength core fields that overlap the crustal field. Previous work, summarized by Langel and Hinze (1998), suggests that in the absence of a field reversal or significant secular variation, these fields will remain unknown. A qualitative approach to the crustal field problem, suggested by Purucker and Whaler (2004), is to visually characterize the global satellite field, and magnetization solutions deduced from that field. Because of the wider spectral content of new satellite solutions (cf. Maus et al., 2005), larger patterns may become apparent, patterns that were not obvious when very band-limited solutions were being examined. By way of analogy, one hopes to be able to differentiate “the

forests from the fields“ by characterizing features at smaller spatial scales (like the “trees and grasses“). This analogy implies that there are features at small scales that give us clues into what is happening at the largest scales. Purucker and Whaler (2004) recognized and characterized two distinctive patterns in the solution of Maus et al. (2005), and in minimum amplitude magnetization models that they developed. The boundaries of these patterns defined long-wavelength features in the lithospheric field not previously recognized because they were obscured by overlap with the core field. These boundaries corresponded to known crustal thickness variations. The major exceptions, the Sahara and most of South America south of the Equator, are known to be regions where direct estimates of crustal thickness and heat flow are sparse.

Another outstanding question is the origin of anomalies that can not be explained by induced or remanent magnetization of known structures in the crust or mantle. For example, Maus et al. (2005) report on prominent stripes in the ocean whose power is centered on spherical harmonic degree 15. These stripes do not correspond to any known oceanic structures. Magnetic fields induced by the regular variations of ionospheric current systems acting on the large-scale conductivity contrast between seawater and rock should also produce quasi-static to regularly varying fields (Tarits and Grammatica, 2000), but they have not yet been isolated. Large scale ocean currents, such as the Antarctic Circumpolar Current, are also expected to produce quasi-static signatures of up to a few nT at satellite altitude (Vivier et al., 2004; Friis-Christensen et al., 2004; Olsen et al., 2004). Because the time-varying nature of these currents is less well-known than those of the tides (Tyler et al., 2003), it has not been possible to isolate these signals from the satellite data.

The proportions of induced, viscous remanent, and high-coercivity remanent magnetization within the crust and upper mantle is also still a matter of debate, especially in the light of the dominant role of high-coercivity remanent magnetization in the Martian crust (Langlais et al., 2004). Recent work on this problem includes that of Maus and Haak (2002).

Also of considerable interest is the importance of distributions of magnetization within the crust which have no signature at satellite altitude (Maus and Haak, 2003). Are such distributions likely to be of practical importance? A long-standing problem is the adequacy of the continental lower crust to produce the observed satellite magnetic signal. Several authors (Shive and Fountain, 1988, but see Kelson et al., 1993) have argued that the magnetic properties of exposed lower crustal sections are inadequate to explain the satellite signal.

Another long-standing problem is the difficulty of extracting North-South magnetic anomalies at all wavelengths, because of the systematic use of polar orbits and along-track filtering of external field effects. This problem has been partly alleviated with the use of comprehensive models, as shown in Figure

9 (Sabaka et al., 2004), and will be further mitigated by the Swarm magnetic field constellation satellites (Friis-Christensen et al., 2004; Olsen et al., 2004).

Finally, there remains a bias in our models introduced by the external field and its induced part, and also a bias introduced by inaccuracies in main field models. These biases will be mitigated by more comprehensive approaches (Olsen et al., 2002) to field modeling, and by the new constellation.

5.4. External fields

Our knowledge of external magnetic fields has also been enhanced by near-Earth satellite missions. Of particular importance is the expansion of the South Atlantic anomaly since the beginning of the space age (Figure 14). This decrease in the field magnitude centered over the South Atlantic is a direct consequence of the growth of reverse flux patches at the core-mantle boundary, and has expanded the area in which routine spacecraft operations are subject to disruption by enhanced particle fluxes (Heirtzler et al., 2002).

Although this review focuses on magnetic fields in the solid Earth, a knowledge of the external field is also important, because the solid-earth researcher needs to be able to model or remove those fields from the observations prior to interpretation. A short listing of important discoveries concerning the quiet-time external field would certainly include: 1) the confirmation of a meridional current system (Maeda et al., 1982) connecting the low-latitude ionosphere and magnetosphere, a current system which appears to close below the altitude of the Ørsted satellite (Sabaka et al., 2004), 2) detailed global views in space and time of the equatorial electrojet (Lühr et al., 2004), and 3) the magnetic effects of plasma enhancements in the low-latitude ionosphere (Lühr et al., 2003). These enhancements of electron density occur North and South of the dip equator in the "crest" region, and are strongest from sunset to midnight. Changes in the magnetic field of as much as 5 nT have been reported during quiet times.

6. An upcoming mission, and its objectives

Several of the outstanding questions outlined in the previous sections require a new satellite mission. Swarm is an ESA Earth Explorer Opportunity mission[13] scheduled for launch in 2009 that is designed to address these questions. It will consist of a constellation of three polar-orbiting satellites optimized for the separation of temporal and spatial variations of the field. The three satellites will be at two altitudes, 450 and 530 km, and the lower pair will provide, for the first time, systematic mapping of magnetic field gradients in near-Earth space (Figure 15). Mapping these gradients, as the

[13] http://www.esa.int/export/esaLP/swarm.html

lower pair travel side-by-side with an average separation of 150 km, will fill the spectral hole between spherical harmonic degrees 60-90 (CHAMP) and 150 (highest quality aeromagnetic surveys). The orbital planes of the upper and lower satellites will drift apart in order to better recover high-degree secular variation and 3-D mantle conductivity. Measurements of the lithospheric field by this mission should allow for a global compilation of the lithospheric magnetic field at scales from 5 to 3000 km to be made. Such a compilation would enable structural and thermo-mechanical interpretations of the crust from top to bottom, and yield a better understanding of how remanent magnetization gives way to induced magnetization in the crust. The mission would also delineate oceanic magnetic stripes laid down during more typical times of reversing polarity, permitting an understanding of first-order plate tectonics in the southern oceans, where marine surveys are currently widely spaced. Measurements of the core field and its secular variation are designed to achieve a higher resolution of core surface flow in space and time, to constrain the role of diffusion and waves, and to predict the short-term evolution of the geodynamo. Measurements of the time-varying external field are expected to allow the development of global transfer functions which would permit the characterization of the 3-D electrical conductivity of the mantle in the 100-1000 km depth range.

7. Conclusion

The joint analysis of ground-based and satellite data is a keystone to future progress in geomagnetism because of their very different distributions in space and in time. However, in order to achieve a new "view" inside the Earth, to study the composition and processes in its interior, or to analyze the Suns' influence within the Earth system, continuous ground and space measurements of the magnetic field are needed. The measurements provided by the different platforms also have practical applications in many different areas, such as resource exploration,space weather, radiation hazards, and navigation.

It should be clear to the reader that the Earth's magnetic field is complicated, with a multitude of sources having overlapping temporal and spatial characteristics. It is also clear that there is the need for a comprehensive separation and understanding of the internal and external processes contributing to the Earth's magnetic fields. Continuous space-borne monitoring of the magnetic field aims to address such needs, and the Swarm mission will offer new insights into the processes operating in the interior and surroundings of our planet.

Acknowledgements

All figures were produced with GMT (Wessel and Smith, 1991). MEP is supported under NASA Contract NAS5-00181. We would like to thank E. Thebault for discussions of Spherical Cap Harmonic Analysis.

References

Acuña, M.H.: 2002, Space-based magnetometers, *Review of Scientific Instruments* **73**, 3717-3736.

Alldredge, L. R.: 1981, Rectangular harmonic analysis applied to the geomagnetic field, *J. Geophys. Res.* **86**, 3021-3026.

Backus, G.E.: 1970, Non-Uniqueness of the external geomagnetic field determined by surface intensity measurements, *J. Geophys. Res.* **75**, 6339-6341.

Balasis, G.: 2004, Identification, classification and separation of F-region currents orbit errors, and instrument noise in CHAMP FGM data using a wavelet technique, *Earth Observation with CHAMP: Results from Three Years in Orbit*, Reigber et al., eds., Springer, Berlin.

Barraclough, D.R.: 1985, A comparison of satellite and observatory estimates of geomagnetic secular variation, *J. Geophys. Res.* **90**, 2523-2526.

Bloxham, J., Zatman, S., Dumberry, M.: 2002, The origin of geomagnetic jerks, *Nature* **420**, 65-68.

Cain, J.C., Hendricks, S.J., Langel, R.A, and Hudson, W.V.: 1967, A proposed model for the International Geomagnetic Reference Field 1965, *J. Geomag. Geoelectr.* **19**, 335-355.

Cain, J.C., Frayser, J., Muth, L., and Schmitz, D.: 1983, The use of MAGSAT data to determine secular variation, *J. Geophys. Res.* **88**, 5903-5910.

Chambodut, A., Schwarte, J., Mandea, M., and Lühr, H.: 2003, The selection of data in main field models, *OIST-4 Proceedings*, DMI Scientific Report 03-09, Stauning, P. et al., eds.,Copenhagen, Denmark, 31-34.

Chambodut, A. and Mandea, M.: 2005, Evidence for Geomagnetic Jerks in Comprehensive Models,*Earth, Planets, Space*, in press.

Chulliat, A. and Hulot, G.: 2000, Local computation of the geostrophic pressure at the top of the core, *Phys. Earth Planet Int.* **117**, 309-328.

Covington, J.: 1993, Improvement of equivalent source inversion technique with a more symmetric dipole distribution model, *Phys. Earth Planet. Int.* **76**, 199-208.

De Santis, A., Falcone, C., and Torta, J.: 1997, Regional Evaluations and Models. SHA vs. SCHA for Modelling Secular Variation in a Small Region Such as Italy, *J. Geomag. Geoelec.* **49**, 359-371.

Eymin-Petot-Tourtollet C.: 2004, Etude des mouvements à la surface du noyau terrestre : du 17ème au 21ème siècle, Thèse IPGP, Paris.

Fox Maule, C., Purucker, M., and Olsen, N.: 2003, Magnetic crustal thickness and heat flow in Antarctica, *Eos Trans. AGU* **84**(46), Fall meet. Suppl., Abstract GP21D-05.

Friis-Christensen, E., De Santis, A., Jackson, A., Hulot, G., Kuvshinov, A., Lühr, H., Mandea, M., Maus, S., Olsen, N., Purucker, M., Rothacher, M., Sabaka, T., Thomson, A., Vennerstrom, S., and Visser, P.: 2004, *Swarm. The Earth's Magnetic Field and Environment Explorers*, ESA SP-1279(6).

Gauss, C.F.: 1839, *Allgemeine Theorie des Erdmagnetismus*, Leipzig.

Gire, C. and Le Mouël, J.-L.: 1990, Tangentially geostrophic flow at the core-mantle boundary compatible with the observed geomagnetic secular variation: the large-scale component of the flow, *Phys. Earth Planet. Int.* **59**, 259-287.

Gire, C., Le Mouël, J.-L., and Ducruix, J.: 1984, Evolution of the geomagnetic secular variation field from the beginning of the century, *Nature* **307**, 349-352.

Haines, G.: 1985, Spherical cap harmonic analysis, *J. Geophys. Res.* **90**, 2593-2598.

Haines, G.: 1990, Regional magnetic field modeling: a review, *J. Geomag. Geoelec.* **42**, 1001-1018.

Halley, E.: 1692, An account of the cause of the change of the variation of the magnetical needle; with an hypothesis of the structure of the internal parts of the Earth, *Phil. Trans. R. Soc. London* **195**, 563-578.

Heirtzler, J.R., Allen, J.H., and Wilkinson, D.C.: 2002, Ever-present South Atlantic anomaly damages spacecraft, *EOS, Trans. AGU* **83**, 165, 169.

Holme, R.: 2000, Modelling of attitude error in vector magnetic data: application to Ørsted data. *Earth Planets Space* **52**, 1187-1197.

Holme, R. and Bloxham, J.: 1996, The treatment of attitude errors in satellite geomagnetic data, *Phys. Earth Planet. Int.* **98**, 221-233.

Holme, R.: 1998, Electromagnetic core-mantle coupling I. Explaining decadal changes in the length of day, *Geophys. J. Int.*, **132**, 167-180.

Holme, R., N. Olsen, M. Rother and H. Lühr: 2003, CO2: A CHAMP magnetic field model, *Proceedings of the First CHAMP Science Meeting*, edited by Chr. Reigber, H. Lühr and P. Schwintzer, Springer Verlag.

Hulot, G., Eymin, C., Langlais, B., Mandea, M., and Olsen, N.: 2002, Small-scale structure dynamics of the geodynamo inferred from Ørsted and MAGSAT satellite data, *Nature* **416**, 620-623.

Hwang, C. and Chen, S.-K.: 1997, Fully normalized spherical cap harmonics: application to the analysis of sea level data from TOPEX/POSEIDON and ERS-1, *Geophys. J. Int.* **129**, 450-460.

Jackson, A., Bloxham, J., and Gubbins, D.: 1993, Time-dependent flow at the core surface and conservation of angular momentum in the coupled core-mantle system, *Dynamics of Earth's Deep Interior and Earth Rotation*, IUGG **12**. AGU Geophysical Monograph, eds. Le Mouël, J.-L., Smylie, D.E., and Herring, T. **72**, 97-107.

Jackson, A., Jonkers, A.R.T., and Walker, M.R.: 2000, Four centuries of geomagnetic secular variation from historical records, *Phil. Trans. R. Soc. London A*, **358**, 957-990.

Jault, D., Gire C., and Le Mouël,J.L.:1988, Westward drift, core motions and exchanges angular momentum between core and mantle, *Nature*, **333**, 353-356.

Jankowski, J. and Sucksdorff, C.: 1996, *Guide for magnetic measurements and observatory practice*, International Association of Geomagnetism and Aeronomy, Int. Assoc. Geomag. Aeronomy, Warsaw.

Jault, D., Hulot, G., and Le Mouël, J.-L.: 1996, Mechanical core-mantle coupling and dynamo modelling, *Phys. Earth Planet. Inter.* **98**, 187-192.

Katanforoush, A. and Shahshahani, M.: 2003, Distributing points on a sphere, *J. Experimental Mathematics* **12**(2), www.expmath.org.

Kelson, P., Bannerjee, S.K., and Teyssier, C.: 1993, The rock magnetic properties of the Arunta block, central Australia and their implications for the interpretation of long-wavelength magnetic anomalies, *J. Geophys. Res.* **98**(B9), 15987-15999.

Kivelson, M.G. and Russell, C.T.: 1995, *Introduction to Space Physics*, Cambridge, 567 pp.

Korte, M. and Haak, V.: 2000, Modelling European Magnetic Repeat Station Data by SCHA in Search of Time-varying Anomalies, *Phys. Earth Planet. Int.* **122**, 205-220.

Korte, M. and Mandea, M.: 2003, Improvements Planned for European Geomagnetic Repeat Stations, *EOS, AGU,* **84**(17), 160.

Langel, R.A., The main geomagnetic field, in *Geomagnetism*,v. 1, 249-512, (ed. Jacobs, J.A., Academic Press, London).

Langel, R.A. and Estes, R.H.: 1985, The near-Earth magnetic field at 1980 determined from Magsat data, *J. Geophys. Res.* **90**, 2495-2510.

Langel, R.A. and Hinze, W.J.: 1998, *The Magnetic Field of the Earth.s Lithosphere: The Satellite Perspective*, Cambridge University Press, Cambridge, 429 pp.

Langlais, B., Ultré-Guérard, P., Vernin, C., Mandea, M., Cohen, Y., and Hulot, G.: 1999, *Ørsted: IPGP commissioning of the OVH magnetometer*, CNES, OERS-RP 0000-0031-IPG, pp. 28.

Langlais, B., Mandea, M., Ultré-Guérard, P.: 2003, High-resolution magnetic field modeling: application to MAGSAT and Ørsted data, *Phys. Earth Planet. Int.* **135**, 77-92.

Langlais, B., Purucker, M., and Mandea, M.: 2004, Crustal magnetic field of Mars, *J. Geophys. Res-Planets*, **109**, E02008, doi:10.1029/2003JE002048.

Le Mouël, J.-L.: 1984, Outer-core geostrophic flow and secular variation of Earth's geomagnetic field, *Nature* **311**, 734-735.

Lühr, H., Rother, M., Maus, S., Mai, W., and Cooke, D.: 2003, The diamagnetic effect of the equatorial Appleton anomaly: Its characteristics and impact on geomagnetic field modeling, *Geophys. Res. Lett.* **30**, 10.1029/2003GL017, 407.

Lühr, H., Maus, S., and Rother, M.: 2004, Noon-time equatorial electrojet: Its spatial features as determined by the CHAMP satellite, *J. Geophys. Res.* **109**(10), 1029/2002JA009656.

Maeda, H., Iyemori, T., Araki, T., and Kamei, T.: 1982, New evidence of a meridional current system in the equatorial ionosphere, *Geophys. Res. Lett.* **9**, 337-340.

Mandea Alexandrescu, M. and Bitterly, J.: 1999, French results of the geomagnetic field repeat station networks measurements, *Bureau Central de Magnétisme Terrestre - Paris* **12**, 43-54.

Mandea, M., Bellanger, E., and Le Mouël, J.-L.: 2000, A geomagnetic jerk for the end of 20th century? *Earth Planet. Sci. Lett.* **183**, 369-373.

Mandea, M. and Macmillan, S.: 2000, International Geomagnetic Reference Field - the eighth generation. *Earth Planets Space* **52**, 1119-1124.

Mandea, M., and Dormy, E.: 2003, Asymmetric behavior of magnetic dip poles, *Earth Planets Space* **55**, 153-157.

Maus, S. and Haak, V.: 2002, Is the long wavelength crustal magnetic field dominated by induced or by remanent magnetisation? *J. Ind. Geophys. Union* **6**(1), 1-5.

Maus, S. and Haak, V.: 2003, Magnetic field annihilator: invisible magnetisation at the magnetic equator, *Geophys. J. Int.* **155**(2), 509-513.

Maus, S., Rother, M., Holme, R., Lühr, H., Olsen, N. and Haak, V.: 2002, First scalar magnetic anomaly map from CHAMP satellite data indicates weak lithospheric field, *Geophys. Res. Lett.* **29**(14), 10.1029/2001GL013685.

Maus, S., Rother, M., Hemant, K., Lühr, H., Kuvshinov, A., and Olsen, N.: 2005, Earth's crustal magnetic field determined to spherical harmonic degree 90 from CHAMP satellite measurements, *Geophys. J. Int.*, in review.

Mayhew, M.A.: 1979, Inversion of satellite magnetic anomaly data, *Geophys. Jour.* **45**, 119-128.

Merrill, R.T., McElhinny, M.W., and McFadden, P.L.: 1996, *The magnetic field of the Earth*, Academic Press, San Diego, pp. 531.

Neubert, T., Mandea, M., Hulot, G., von Frese, R., Primdahl, F., Jorgenson, J.L., Friis-Christensen, E., Stauning, P., Olsen, N., and Risbo, T.: 2001, High-Precision geomagnetic field data from the Ørsted satellite, *Eos, Trans. AGU* **82**, 81,87.

Newitt, L.R., Barton, C.E., and Bitterly, J.: 1996, *Guide for Magnetic Repeat Station Surveys*, IAGA.

Newitt, L.R., Mandea, M., McKee, L.A., and Orgeval, J.J.: 2002, Recent acceleration of the north magnetic pole linked to magnetic jerks, *Eos, Trans. AGU* **83**, 381, 388.

O'Brien, M.S., and Parker, R.L.: 1993, Regularized geomagnetic field modeling using monopoles, *Geophys. J. Int.* **118**, 566-578.

Olsen, N.: 2002, A model of the geomagnetic field and its secular variation for epoch 2000 estimated from Orsted data, *Geophys. J. Int.* **149**, 454-462.

Olsen, N., Holme, R., Hulot, G., Sabaka, T., Neubert, T., Tøffner-Clausen, L., Primdahl, F., Jørgensen, J., Léger, J.-M., Barraclough, D., Bloxham, J., Cain, J., Constable, C., Golovkov, V., Jackson, A., Kotzé, P., Langlais, B.,

Macmillan, S., Mandea, M., Merayo, J., Newitt, L., Purucker, M., Risbo, T., Stampe, M., Thompson, A., and Voorhies, C.: 2000, Ørsted Initial Field Model, *Geophys. Res. Lett.* **27**, 3607-3610.

Olsen, N., Moretto, T., and Friis-Christensen, E.: 2002, New approaches to explore the Earth's magnetic field, *J. of Geodynamics* **33**, 29-41.

Olsen, N., Toffner-Clausen, L., Sabaka, T.J., Brauer, P., Merayo, J.G., Jorgensen, J.L., Léger, J.-M., Nielsen, O.V., Primdahl, F., and Risbo, T.: 2003, Calibration of the Ørsted vector magnetometer, *Earth Planets Space* **55**, 11-18.

Olsen, N., Friis-Christensen, E., Hulot G., Korte, M., Kuvshinov, A., Lesur, V., Lüer, H., Macmillan, S., Mandea, M., Maus, S., Purucker, M., Reigber, C., Ritter, P., Rother, M., Sabaka T., Tarits P., and Thomson, A., 2004: Swarm End-to-End mission performance simulator study, ESA Contract No. 17263/03/NL/CB, DSRI Report.

Pais, A., and Hulot G.: 2000, Length of day decade variations, torsional oscillations and inner core superrotation: evidence from recovered core surface zonal flows, *Phys. Earth Planet. Inter.*, **118**, 291-316.

Parker, R.L.: 1994, *Geophysical Inverse Theory*, Princeton University Press, Princeton, 386 pp.

Press, W.H., Teukolsky, S.A., Vetterling, W.T., and Flannery, B.P.: 1992, *Numerical recipes in C, the art of scientific computing*, second edition, Cambridge University Press, New York, 71-89.

Primdahl, F.:2000, *Resonance magnetometers*, in Pavel Ripka (ed.) *Magnetic Sensors and Magnetometers*, Artech House Inc., ch.7, 267-304.

Purucker, M.E., Sabaka, T.J., and Langel, R.A.: 1996, Conjugate gradient analysis: a new tool for studying satellite magnetic datasets, *Geophys. Res. Lett.* **23**, 507-510.

Purucker, M., McCreadie, H., Vennerstroem, S., Hulot, G., Olsen, N., Lühr, H., and Garnero, E.: 2002, Highlights from AGU's virtual session on new magnetic field satellites. *Eos Trans. AGU* **83**, 368.

Purucker, M. and Whaler, K.: 2003, Merging satellite and aeromagnetic data over Europe, the North Atlantic, and the Arctic, *Second CHAMP Science Meeting*, Potsdam, Germany.

Purucker, M.: 2004, Annihilators at Mars: Are there alternative but reasonable magnetization distributions in the Martian crust that explain the MGS magnetic field observations, *Eos Trans. AGU*, 85(17), Jt. Assem.. Suppl., Abstract P33A-01.

Purucker, M. and Whaler, K.: 2004, Recognizing the longest wavelength lithospheric magnetic signals obscured by overlap with the core field, *Eos Trans. AGU*, 85(47), Fall Meet. Suppl., Abstract GP31A-0821

Ravat, D, Ghidella, M., Korhonen, J., Maus, S., McLean, S., and Reeves, C.: 2003, Towards the World Digital Magnetic Anomaly Map (WDMAM), *Eos Trans. AGU*, 84(46), Fall Meet. Suppl., Abstract GP21D-01.

Ripka, P. (ed).: 2001, Magnetic sensors and magnetometers, Artech House, Boston, pp. 494.

Roberts, P.H. and Scott., S.: 1965, On the analysis of the secular variation, *J. Geomag. Geoelectr.* **17**, 137-151.

Risbo, T., Jorgensen, J., and Primdahl, F.: 2003, Ørsted calibration mission, status and overview, *OIST-4 Proceedings*, DMI Scientific Report 03-09, Stauning, P. et al., eds., Copenhagen, Denmark,313-316.

Runcorn, K.: 1975, On the interpretation of lunar magnetism, *Phys. Earth Planet. Int.* **10**, 327-335.

Sabaka, T.J., Olsen, N., Langel, R.A.: 2002, A comprehensive model of the quiet-time, near-Earth magnetic field: phase 3, *Geophys. J. Int.* **151**, 32-68.

Sabaka, T., Olsen, N., and Purucker, M.: 2004, Extending Comprehensive Models of the Earth's magnetic field with Ørsted and CHAMP data, *Geophys. J. Int.*, in press.

Shive, P. and Fountain, D.: 1988, Magnetic mineralogy in an Archean crustal section: implications for crustal magnetization, *J. Geophys. Res.* **93**B, 12177-12186.

Smith, P.: 1969, *Petrus Peregrinus: 1269, EPISTOLA. The beginning of experimental studies of magnetism in Europe*, Earth Science Reviews/Atlas, Elsevier, A11-A17.

Snare, R.C.: 1998, A History of Vector Magnetometery in Space, in Measurement techniques in space plasmas–fields, Geophys. Monograph 103, (Pfaff, R., Borovsky, J.E., and D.T. Young, eds), Amer. Geophys. Union, Washington, D.C., 101-114.

Stacey F.D.: 1992, *Physics of the Earth*, 3rd edn., Brisbane, Qld., Brookfield Press.

Tarantola, A.: 1987, *Inverse Problem Theory*, Elsevier. New York.

Tarits, P. and Grammatica, N: 2000, Electromagnetic induction effects by the solar quiet magnetic field at satellite altitude, *Geophys. Res. Lett.*, 27, 4009-4012

Thébault E., Scott, J.J., Mandea, M., Hoffbeck, J.P.: 2004, A new proposal for Spherical Cap Harmonic modelling, *Geophys. J. Int.*, 159, 83-103.

Thébault E., Scott, J.J., Mandea, M.: 2005, Revised Spherical Cap Harmonic Analysis (R-SCHA): Validation and Properties, *Geophys. J. Int.*, in review.

Tyler R.H., Mysak, L.A., and Oberhuber, J.M.: 1997, Electromagnetic fields generated by a three dimensional global ocean circulation, *J. Geophys. Res.*, 102, 5531-5552.

Tyler R.H., Maus, S., and Lühr, H.: 2003, Satellite observations of magnetic fields due to ocean tidal flow, *Science*, 299, 239-241.

Van der Sluis, A. and Van der Vorst, H.A.: 1987, Numerical solution of large, sparse linear algebraic systems arising from tomographic problems, in

Seismic Tomography, edited by G. Nolet, Reidel, Dordrecht, Holland, Chapter 3, 49-83.

Vivier F., Maier-Reimer, E., and Tyler, R.H.: 2004, Simulations of magnetic fields generated by the Antarctic Circumpolar Current at satellite altitude: Can geomagnetic measurements be used to monitor the flow?, *Geophys. Res. Lett.* **31**, L10306, doi:10.1029/2004GL019804.

Wardinski, I., and Holme R.: 2004, Secular variation and core–surface flows between 1980 and 2000, 9th *Symposium on Study of the Earth's Deep Interior*

Wasilewski, P.J., and Mayhew M.A.: 1992, The Moho as a magnetic boundary, revisited, *Geophys. Res. Lett.* **19**, 2259-2262.

Wessel, P. and Smith, W.H.F.: 1991, Free software helps map and display data, *EOS Trans. AGU* **72**, 441.

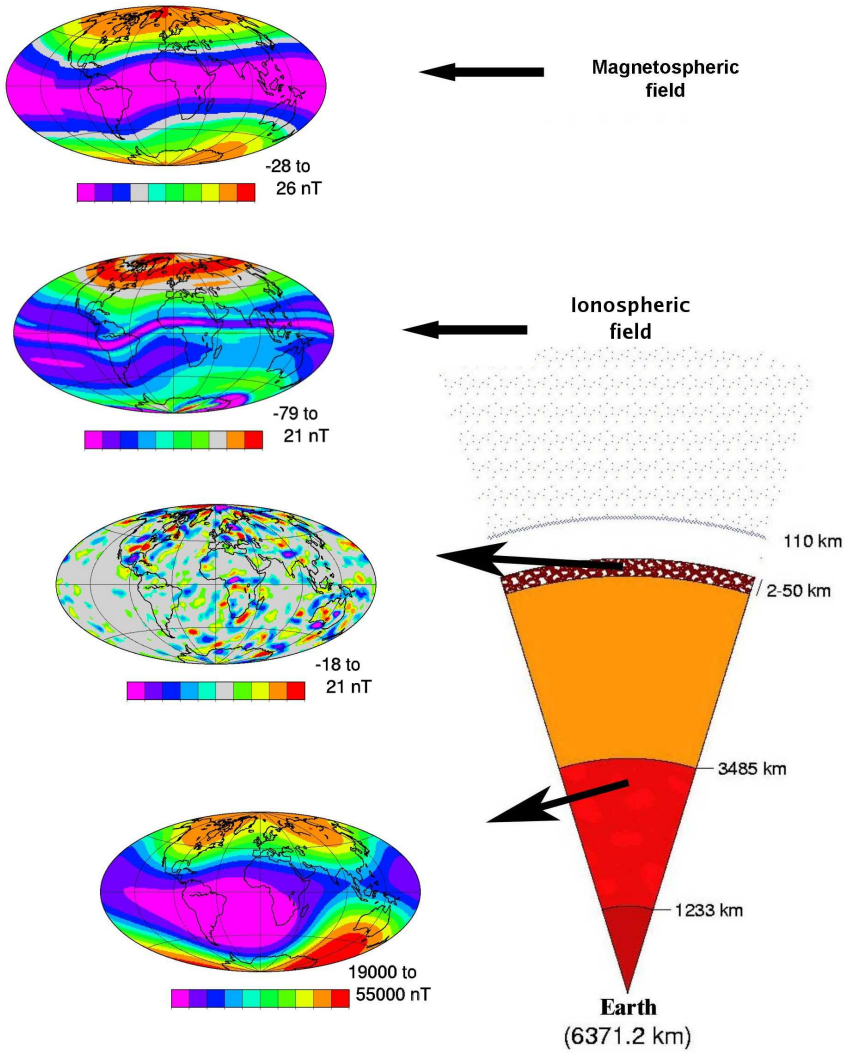

Figure 1. Dominant magnetic fields and their associated source regions within the Earth's system, including those originating in the core (bottom), lithosphere (2nd from bottom), ionosphere (2nd from top) and magnetosphere (top). The core field is from 2002 and is the scalar intensity of the main field between spherical harmonic degree 1 and 13. The lithospheric field in the direction of the main field is shown between spherical harmonic degrees 15 and 65. The ionospheric and magnetospheric fields are from 1330 Local Time on 5 January 2002 and again are the fields in the direction of the main field. Grey scales represent fields between -2 and 2 nT. All fields are calculated at satellite altitude, in this case 400 km, and represent model output from the Comprehensive Model (Sabaka et al., 2004). Hammer projections.

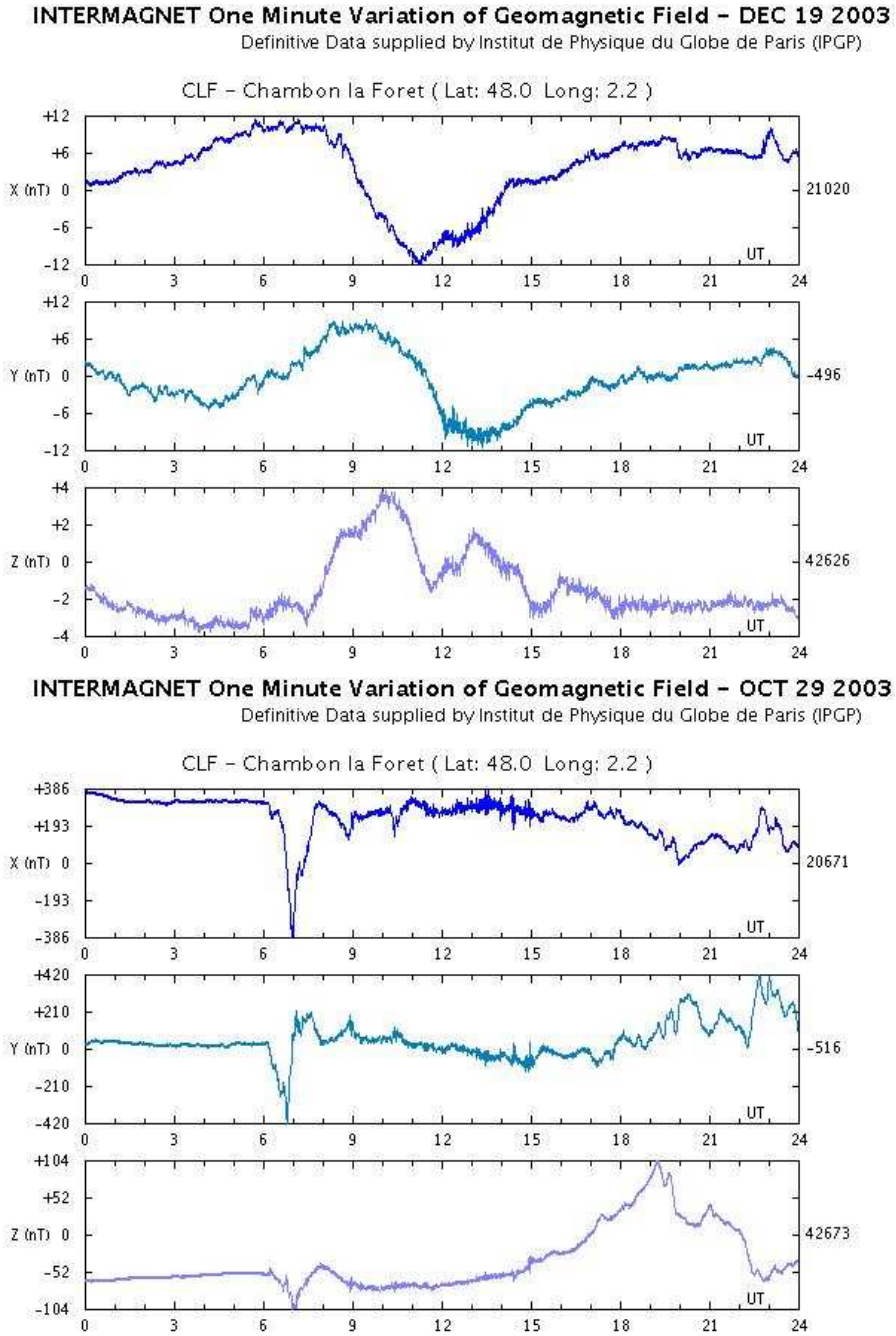

Figure 2. Daily variations of the Earth's magnetic field in nT at Chambon la Foret Observatory (France): (*top*) on a quiet day and (*bottom)* on a disturbed day. X is the north component, Y is the East component, and Z is the vertical component.

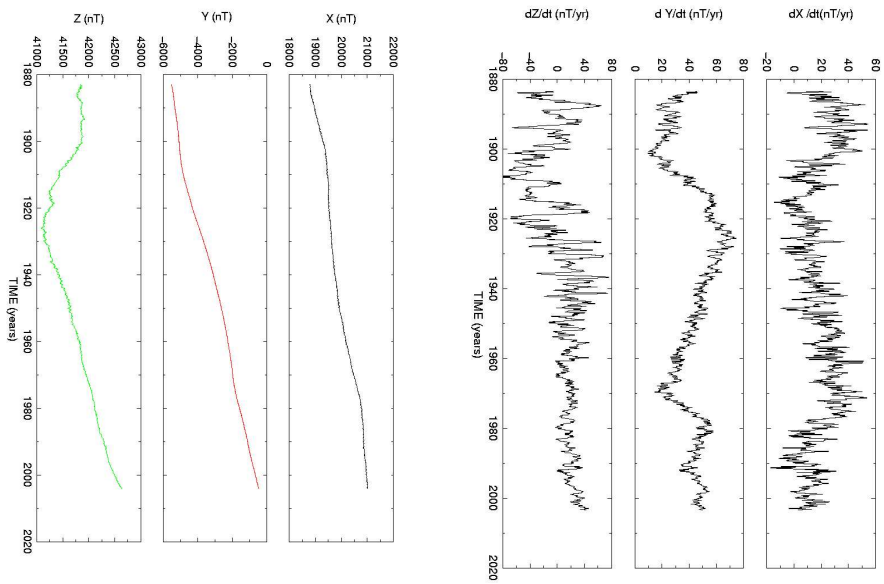

Figure 3. Temporal variations of the three orthogonal components of the Earth's magnetic field at Chambon la Foret Observatory (France): (*top*) magnetic field and (*bottom)* secular variation. Both sets of figures extend from January 1883 to December 2003.

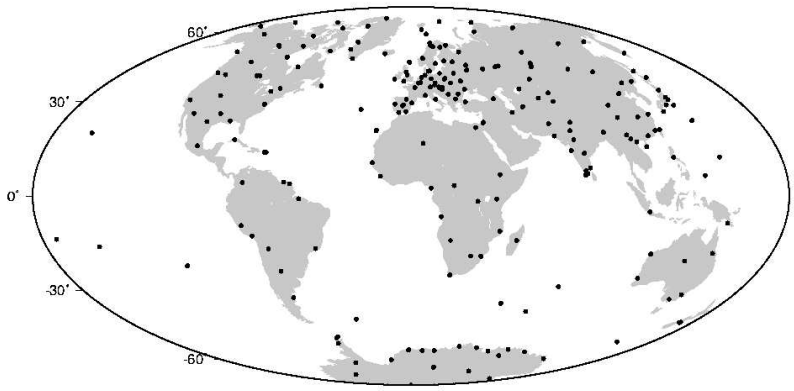

Figure 4. Spatial distribution of magnetic observatory data collected between 1960 and 2000. Hammer projection.

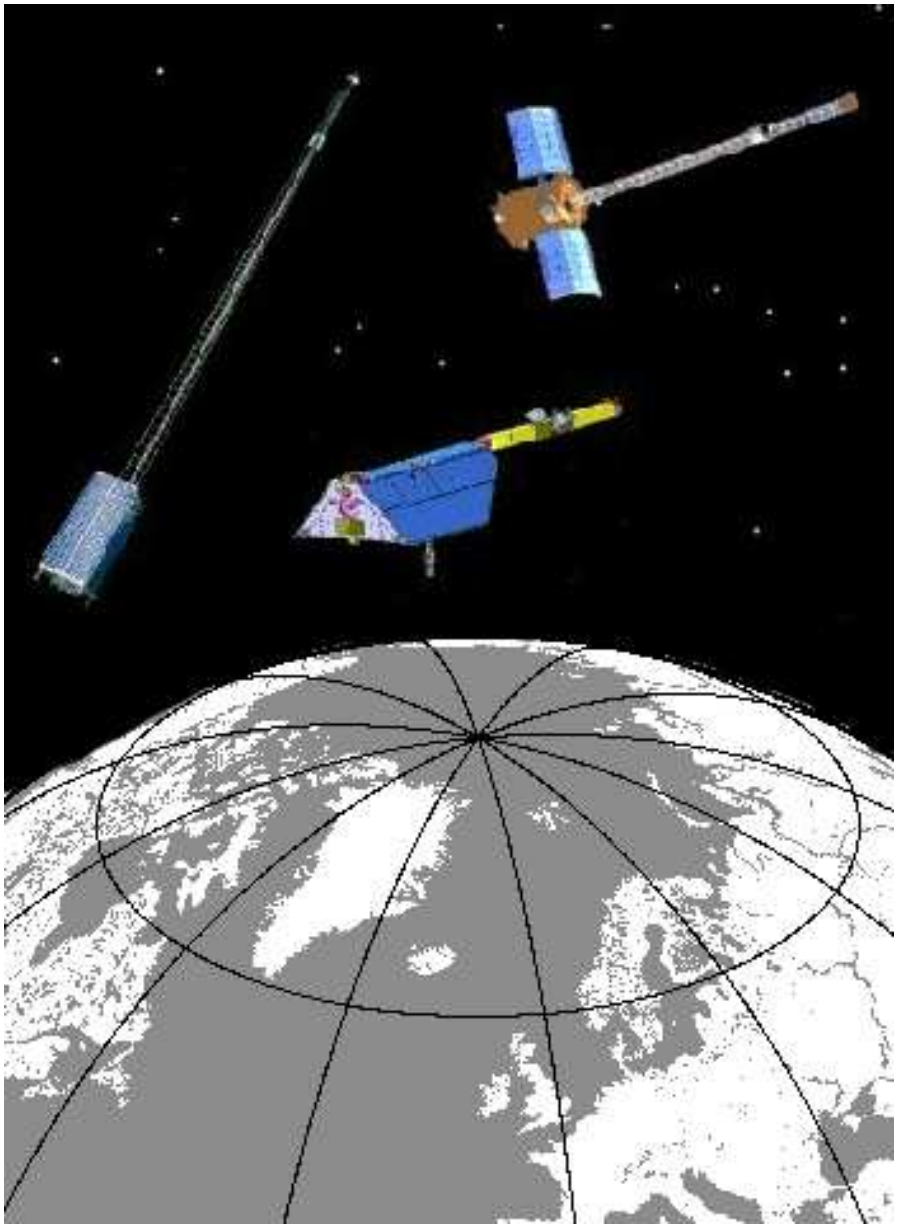

Figure 5. Ørsted (left), CHAMP (center), and SAC-C (top right), showing their shapes, and in flight orientations. All three magnetic field satellites involved international collaborations. In the case of Ørsted, Denmark led an international team including the U.S. and France. CHAMP was a German-led mission that included French, Danish, and U.S. instruments. SAC-C was a joint Argentine-U.S. mission that involved substantial contributions from Denmark.

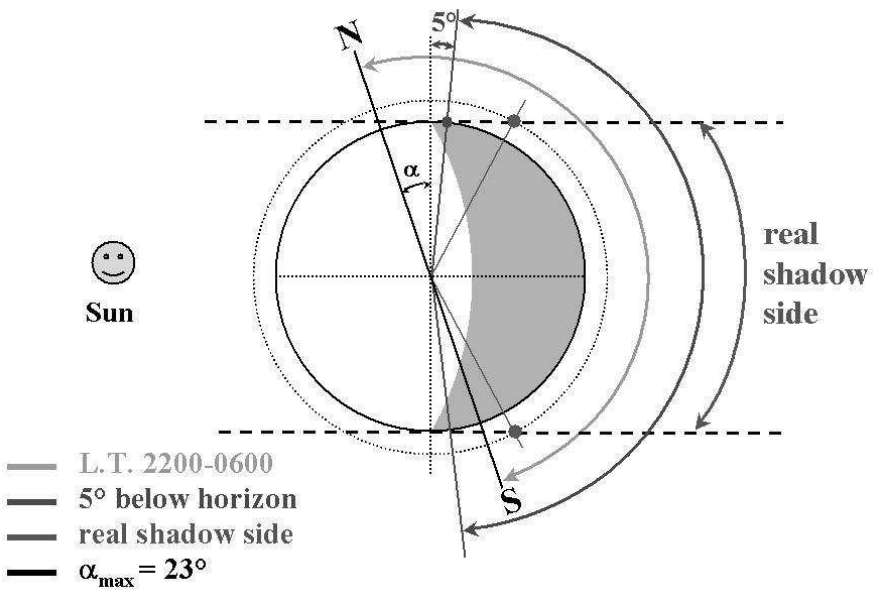

Figure 6. Different night-side definitions often used in data selection. α is the inclination of the equator to the orbital plane.

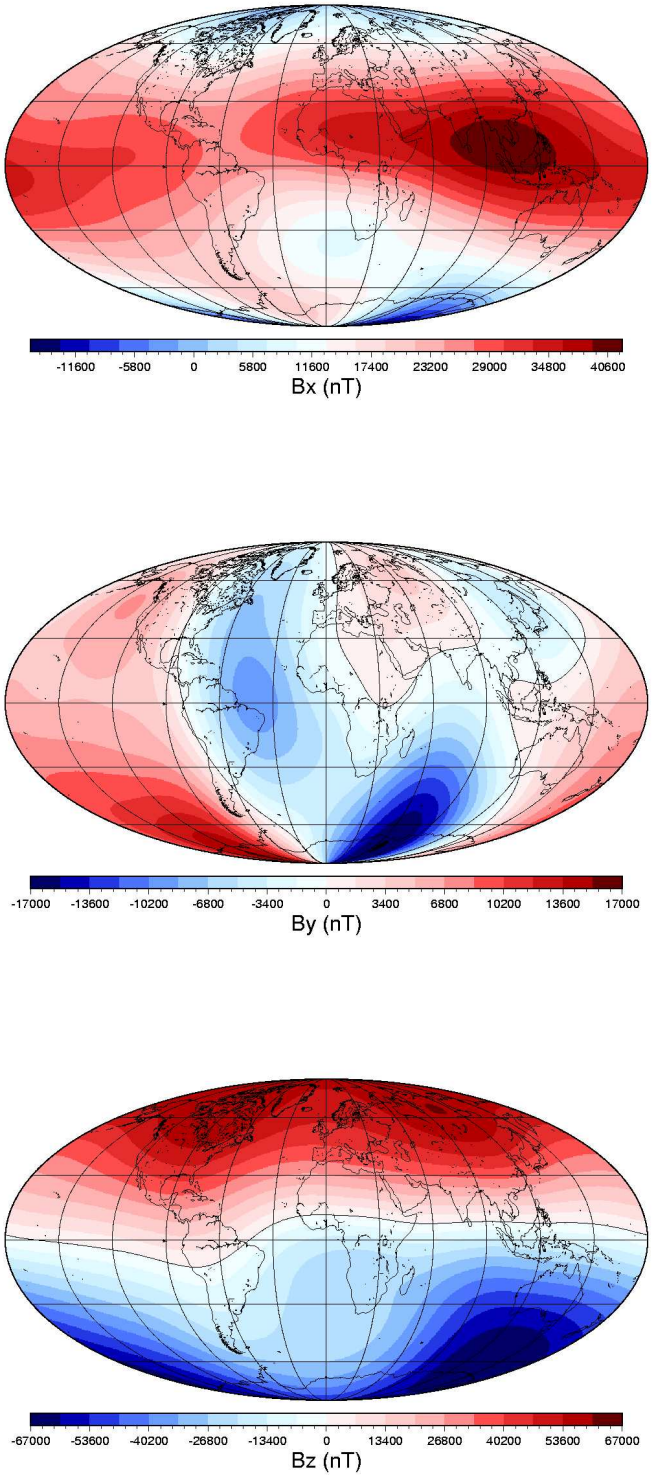

Figure 7. The main field components B_x, B_y, B_z at the Earth's surface (Epoch: 2001) for an Ørsted and CHAMP model utilizing a SAC-C ring current (RC) index (Olsen et al., 2002).

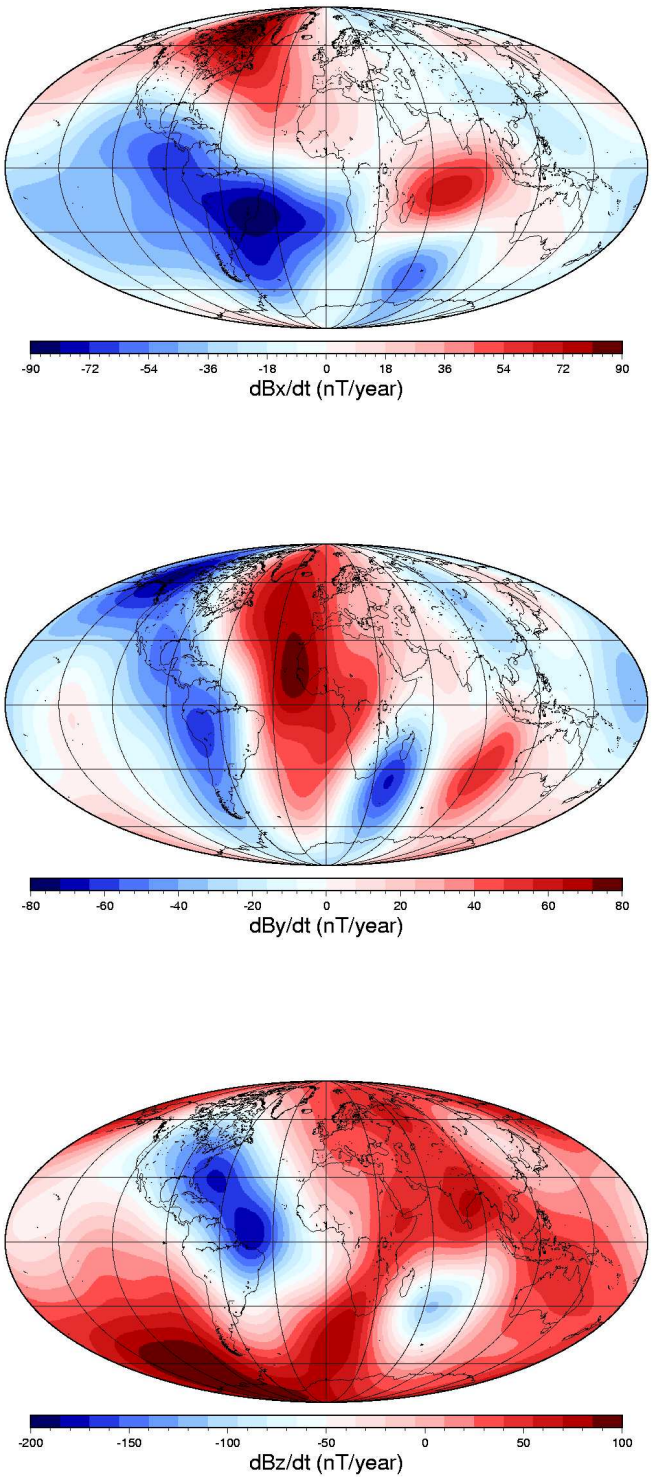

Figure 8. The secular variation components $\dot{B}_x, \dot{B}_y, \dot{B}_z$ at the Earth's surface (Epoch: 2001) for an Ørsted and CHAMP model utilizing a SAC-C ring current (RC) index (Olsen et al., 2002).

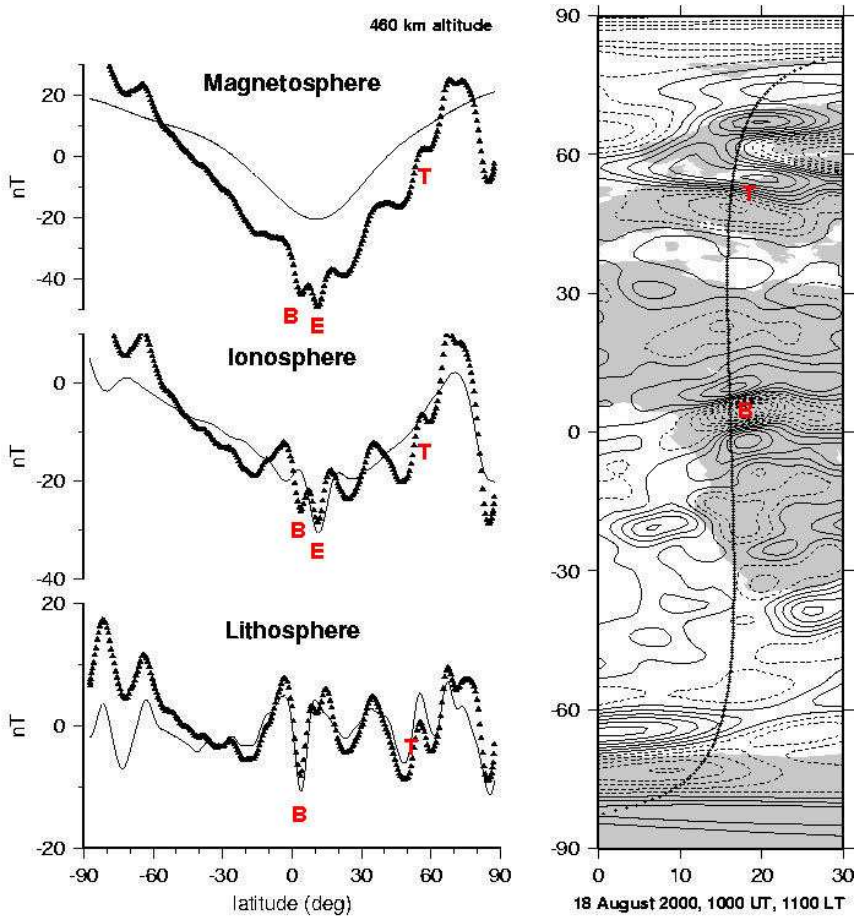

Figure 9. Residual progression versus geographic latitude after magnetic fields from the three main source regions are removed with comprehensive model (Sabaka et al., 2004). This profile shows the Scalar field B of a CHAMP ascending (North-going) pass on 18 August 2000 beginning at 1000 UT and crossing the equator at 15° W and 1100 LT. Magnetically quiet conditions prevailed, with $Kp = 0^+$ for this period, $Kp = 0^+$ for the previous three-hour period, $Dst = -3$ nT, and $|d(Dst)/dt| \leq 4$ nT·hour^{-1}. For a given panel, the symbols represent residuals with respect to the main field (up to degree 13) plus all fields labeled in the panels above; the line is the prediction from the field component labeled in the current panel. The figure on the right shows the location of the subsatellite point and includes a contour map of the scalar field B originating in the lithosphere from the Comprehensive model (C.I. = 2 nT, dashed lines indicate negative B). The equatorial electrojet (Lühr et al., 2004) near the geographic equator (E) is in close proximity to, but distinct from, the Bangui lithospheric anomaly (B). Note also the Tornquist-Teisseyre structure (T), a first-order litho-tectonic feature encompassing both the upper and lower crust in Europe.

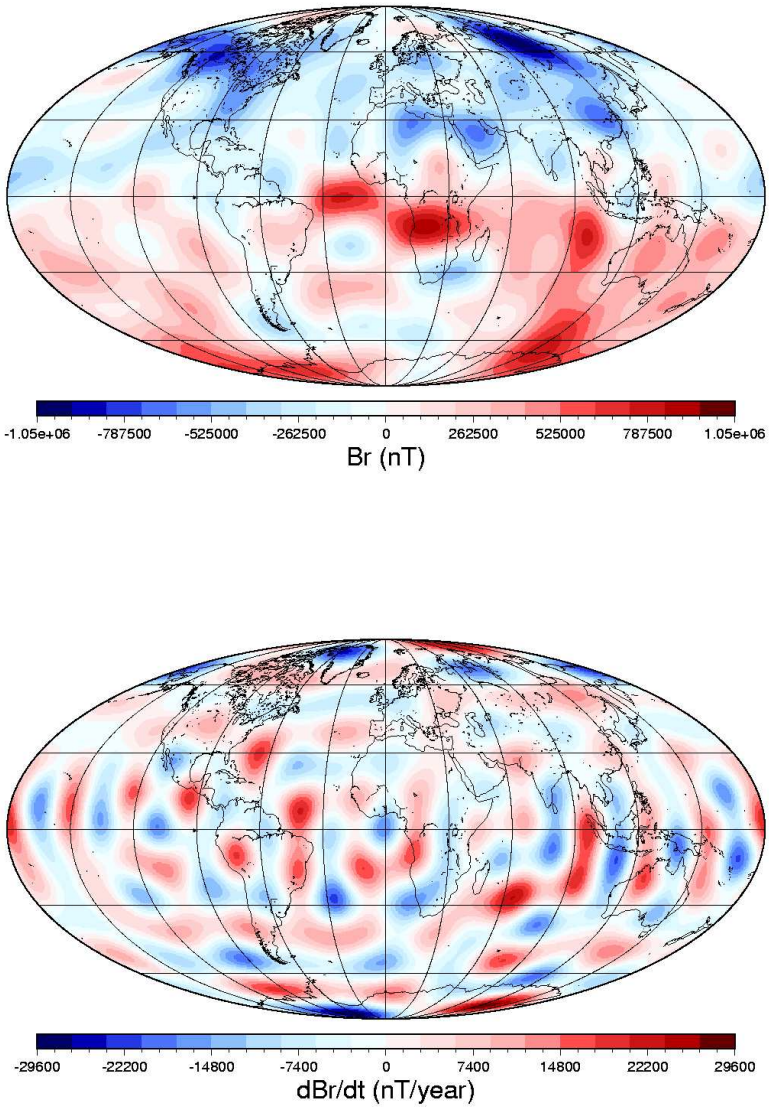

Figure 10. The main field component B_r (*top*), and its secular variation $\dot{B}_r$ (*bottom*) at the core-mantle boundary. Epoch: 2001, and based on the model of Olsen et al. (2002).

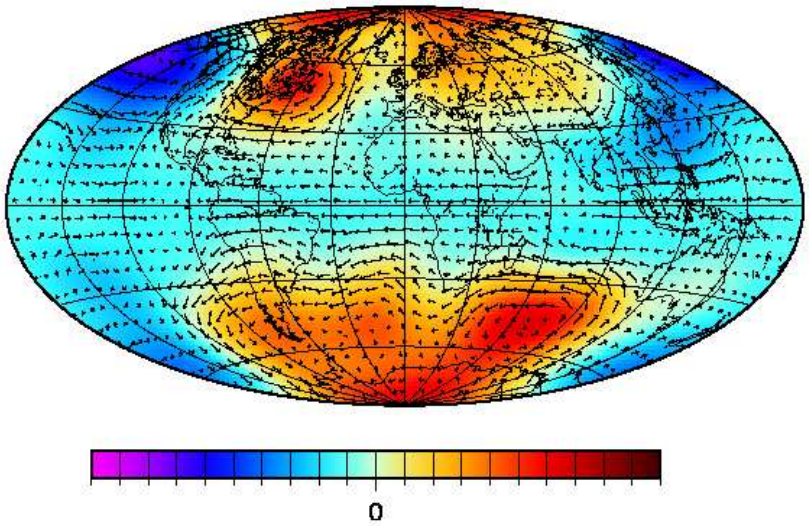

Figure 11. Fluid motion inferred at the core-mantle boundary (after Eymin-Petot-Tourtollet, 2004). Color scale for the dynamic pressure is from -1400 to 1400 Pa, and the longest arrow represents motion of 39 km/yr.

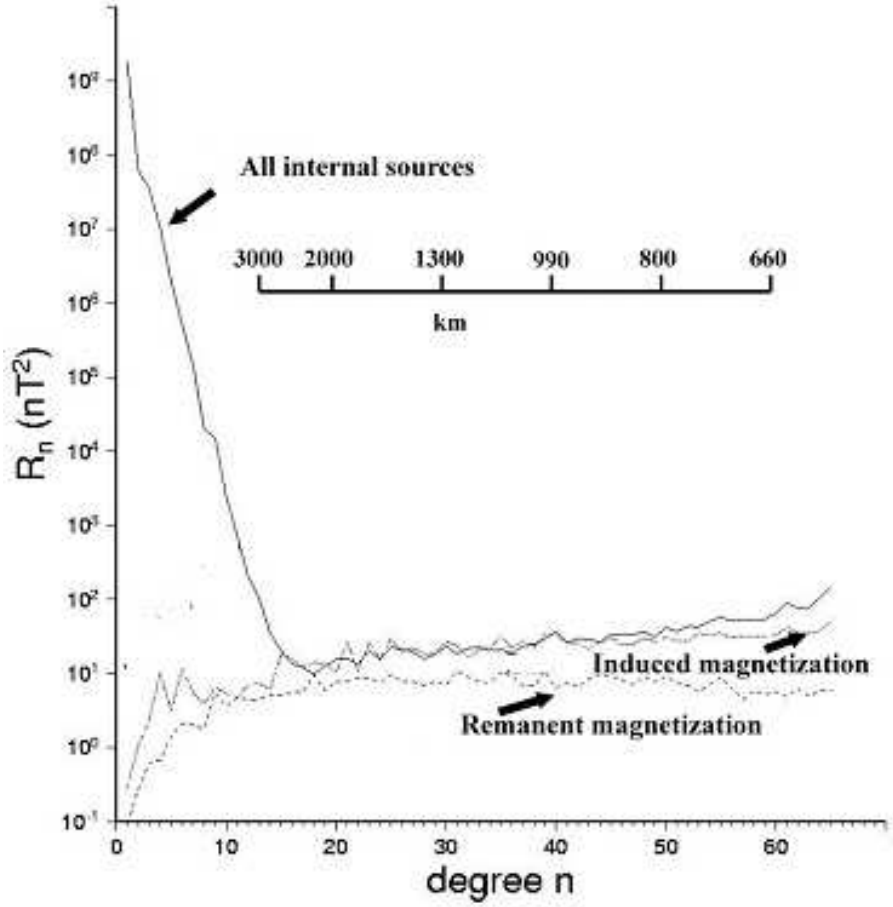

Figure 12. Comparison of the Lowes-Mauersberger (R_n) spectra at the surface of the Earth for a variety of internal fields as a function of spherical harmonic degree. Rn is the mean square amplitude of the magnetic field over a sphere produced by harmonics of degree n. The terrestrial spectrum of all internal sources comes from Sabaka et al. (2004), the terrestrial induced spectrum is derived from Fox Maule et al. (2003), and the terrestrial remanent magnetization spectrum (of the oceans, and hence a minimum value) was derived from Dyment and Arkani-Hamed (1998).

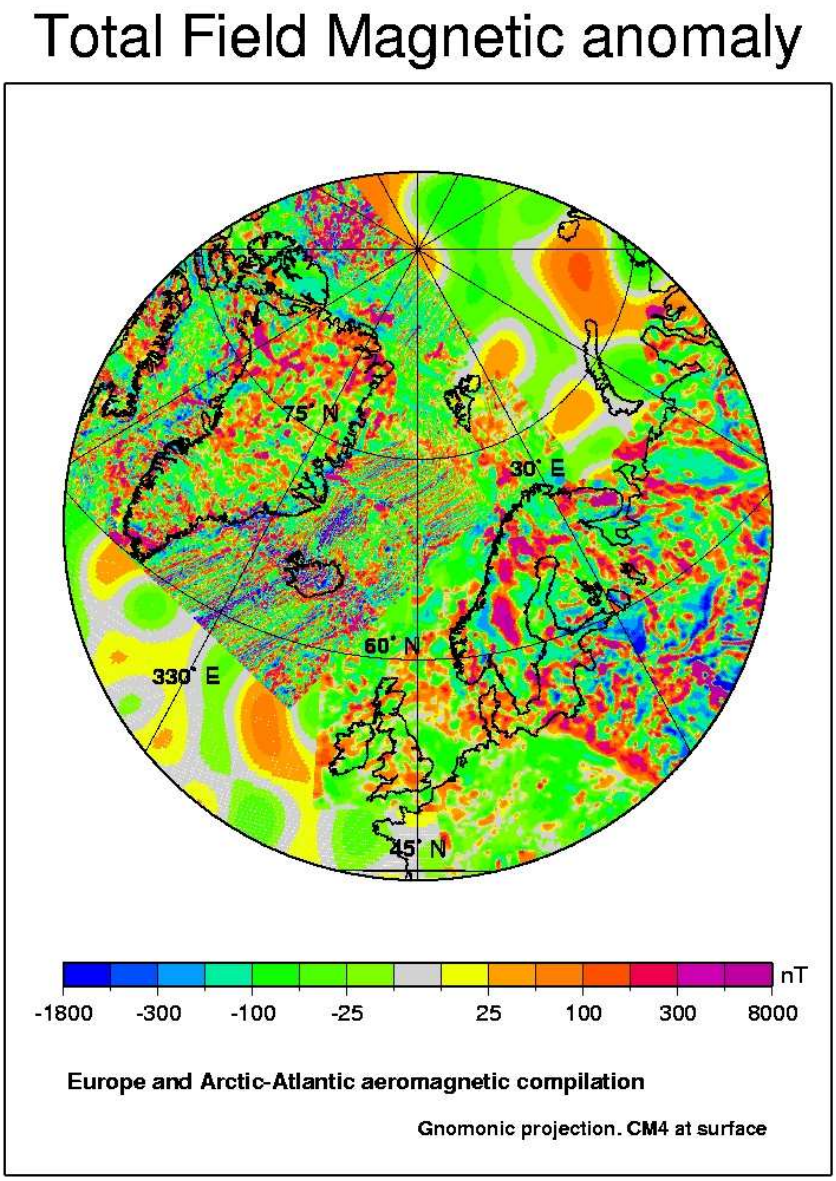

Figure 13. Merged satellite and aeromagnetic-marine magnetic map of Europe, the North Atlantic and the Arctic (Purucker and Whaler, 2003). The aeromagnetic-marine maps contain wavelengths between 10 and 500 km, although wavelengths in excess of 200 km are significantly less robust. The satellite map contains wavelengths in excess of 800 km (spherical harmonic degree 50). The new Swarm satellite magnetic field constellation is designed to fill the spectral gap between 300 and 800 km wavelength, and provide a top to bottom view of the Earth's magnetic crust. CM4 stands for Comprehensive Model: Version 4 (Sabaka et al., 2004).

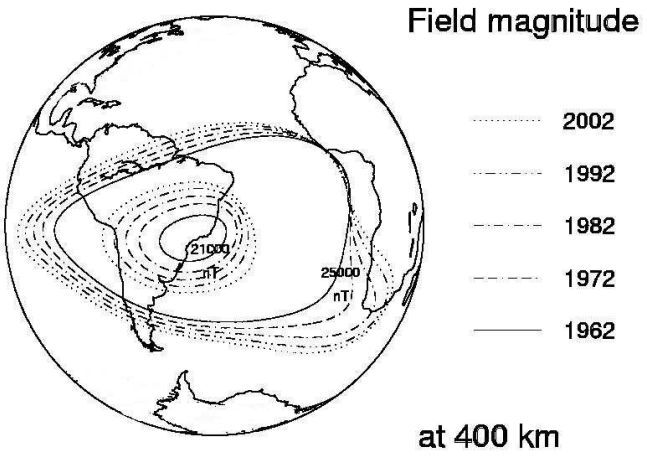

Figure 14. Expansion of the South Atlantic anomaly in near-Earth space since the beginning of the space age. The magnitude of the magnetic field at 400 km is shown at 10 year increments between 1962 and 2002 based on the Comprehensive model of Sabaka et al. (2004).

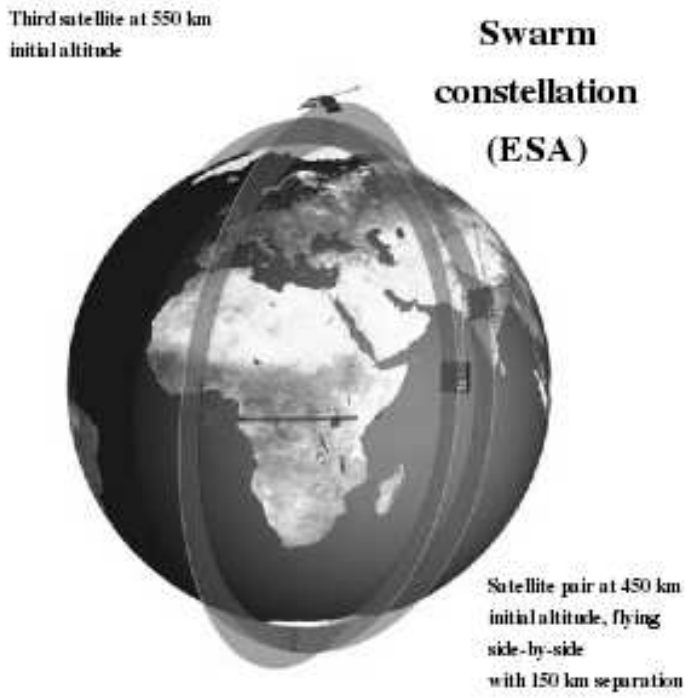

Figure 15. Schematic view of the Swarm constellation.